

# Aerosol-Induced Closure of Marine Cloud Cells: Enhanced Effects in the Presence of Precipitation

Matthew W. Christensen<sup>1</sup>, Peng Wu<sup>1</sup>, Adam C. Varble<sup>1</sup>, Heng Xiao<sup>1</sup>, and Jerome D. Fast<sup>1</sup>

<sup>1</sup>Atmospheric Science & Global Change Division, Pacific Northwest National Laboratory, Richland, WA 99354, Washington, USA

**Correspondence:** Matthew W. Christensen (matt.christensen@pnnl.gov)

**Abstract.** The Weather Research Forecasting (WRF) V4.2 model is configured within a Lagrangian framework to quantify the impact of aerosols on evolving cloud fields. ~~Simulations~~ Kilometer-scale simulations employing realistic meteorological boundary conditions are based on 10 case study days offering diverse meteorology during the Aerosol and Cloud Experiments in the Eastern North Atlantic (ACE-ENA). ~~Cloud and aerosol retrievals in observations from aircraft measurements,~~ Measurements from aircraft, the ground-based Atmosphere Radiation Measurement (ARM) ~~data site~~ data site at Graciosa Island in the Azores, and A-Train and geostationary satellites are ~~in-utilized for validation, demonstrating~~ good agreement with the ~~simulations~~ WRF-simulated cloud and aerosol properties. Higher aerosol concentration leads to suppressed drizzle and increased cloud water content in all case study days. These changes lead to larger radiative cooling rates at cloud top, enhanced vertical velocity variance, and increased vertical and horizontal wind speed near the base of the lower-tropospheric inversion. As a result, marine cloud cell area expands, narrowing the gap between shallow clouds and increasing cloud optical thickness, liquid water content, and the top-of-atmosphere outgoing shortwave flux. While similar aerosol effects are observed in lightly to non-raining clouds, they tend to be smaller by comparison. These ~~results~~ simulations show a strong link between cloud cell area expansion and the radiative adjustments caused by liquid water path and cloud fraction changes. ~~These adjustments scale by~~ The adjustments are positive and scale as 74% and 51%, respectively, relative to the Twomey effect. ~~Given the limitations of traditional global climate model resolutions,~~ While higher resolution large eddy simulations may provide improved representation of cloud-top mixing processes, these results emphasize the importance of addressing mesoscale cloud-state transitions ~~at kilometer-scale resolutions or higher should be of utmost importance in accurately quantifying in the quantification of~~ aerosol radiative forcing that cannot be attained from traditional climate models.

## 1 Introduction

20 The surface temperature of Earth is kept cooler by the presence of low-level clouds, in particular stratocumulus. It has been estimated that a mere increase of about 4% in their global coverage would be enough to offset the radiative warming due to a doubling of atmospheric carbon dioxide (Randall et al., 1984). Aerosols, commonly emitted alongside greenhouse gases have the potential to decrease cloud droplet size and create more numerous ~~cloud~~ droplets that effectively suppress precipitation and moisten the boundary layer (Albrecht, 1989). This process can increase the vertical and horizontal extents of ~~cloud~~ clouds as

25 well as their lifetime (Albrecht, 1989; Pincus and Baker, 1994; Bretherton et al., 2007; Christensen et al., 2020). However, an  
increase in aerosol concentration can also ~~desiccate cloud through an increase in~~ result in cloud desiccation due to enhanced  
cloud-top entrainment caused by more effective evaporation in polluted clouds (Ackerman et al., 2004; Small et al., 2009) or  
through reduced cloud droplet sedimentation (Bretherton et al., 2007). These processes can even modify the cellular structure  
of clouds through changing cloud fraction (Rosenfeld et al., 2006). However, the strength and sign of the cloud radiative effect  
30 depends on a multitude of meteorological factors such as lower ~~troposphere-tropospheric~~ stability and humidity, precipitation  
state (Chen et al., 2014), and the time-scale for which clouds have been polluted (Wang and Feingold, 2009). These complex  
relationships result in poor understanding and large uncertainty in estimates of rapid cloud adjustments to changes in aerosol  
concentration (Bellouin et al., 2020), the so-called aerosol-cloud lifetime effect (Albrecht, 1989). It is critical to quantify and  
resolve process-scale cloud physics impacting rapid adjustments in order to improve estimates of aerosol radiative forcing at  
35 global-scales (Seinfeld et al., 2016).

A preponderance of evidence linking aerosol and cloud radiative effects to the mesoscale structure of clouds has been  
growing in the literature over the past couple of decades (Rosenfeld et al., 2006; Wood, 2012; Christensen and Stephens,  
2012; Eastman et al., 2021). Stratocumulus can exhibit cellular structures which appear closed or open with hexagonal-like or  
honeycomb shapes that organize on scales ranging from 10 – 50 km (Wood, 2005). The impact of aerosol on precipitation,  
40 as proposed by ~~(Rosenfeld et al., 2006)~~ Rosenfeld et al. (2006), can reverse the direction of the wind flow through the vertical  
extent of the marine boundary layer, doubling cloud cover and converting cloud structure from open to closed cells. Eastman  
et al. (2021) observed that stronger surface winds and lower cloud droplet concentrations are typical prior to the transition  
of closed to open cells. Weather Research and Forecasting (WRF) model simulations from Zhou et al. (2018) indicate that  
moisture stratification and precipitation tend to increase horizontal cloud scales by enhancing updraft buoyancy via increased  
45 latent heating. Additionally, longwave radiative cooling near cloud top plays a crucial role in increasing horizontal cloud scales,  
and sub-cloud moist cold pools tend to respond to, rather than determine, mesoscale variability. A Lagrangian framework has  
been shown to be effective in capturing upstream conditioning on developing clouds (Lewis et al., 2023) as well as to be  
used to quantify cloud lifetime, and track changes in cloud microphysics associated with changes in aerosol concentration and  
meteorological conditions (Christensen et al., 2020, 2023).

50 The shortwave cloud radiative effect of transforming open to closed stratocumulus cells was estimated to be as large as 109  
W/m<sup>2</sup> in a composite of 50 case studies from MODIS observations from ~~(Goren and Rosenfeld, 2014)~~ Goren and Rosenfeld (2014)  
. Goren and Rosenfeld (2014) decomposed the aerosol indirect effect into the Twomey effect (the enhancement in shortwave  
cloud albedo caused by increasing cloud droplet concentration for fixed changes in liquid water path), and rapid adjustments  
containing liquid water path and cloud fraction changes. These were estimated to be approximately 26%, 32%, and 42%, re-  
55 spectively. Here, we also quantify cloud water path and fraction adjustments but using a regression technique following Quaas  
et al. (2008) applied to kilometer-scale WRF model simulations of marine stratocumulus. We utilize a Lagrangian framework  
to capture the evolution of low-level clouds and examine how their cellular patterns change over time in order to answer the  
following research questions:

- To what extent does a change in aerosol concentration modify the area and spacing between cloud cells?

- 60 – How does the aerosol indirect radiative effect vary over diverse meteorological conditions?
- How does changing PBL and microphysics schemes affect the aerosol indirect effect?
- How do liquid water path and cloud fraction adjustments compare to the Twomey effect?

To answer these questions we first describe the details of the data sets used in this study (section 2), set up several case study experiments in WRF that utilize a Lagrangian framework (section 3), and conclude with an assessment of the aerosol radiative forcing (sections 4 and 5).

## 2 Observational Data

The U.S. Department of Energy Atmosphere Radiation Measurement (ARM) program has been providing continuous measurements of cloud properties at Graciosa Island in the Azores for over a decade. This location is ideal for studying mesoscale structure (Jensen et al., 2021), turbulence (Ghate and Cadeddu, 2019), and aerosol-cloud interactions (Zheng et al., 2022b; 70 Christensen et al., 2023; Varble et al., 2023) in marine stratocumulus clouds. Ground-based measurements from ARM, aircraft measurements from the Aerosol and Cloud Experiments in the Eastern North Atlantic (ACE-ENA; Wang et al., 2022), and satellite observations from geostationary and polar orbits are used to evaluate WRF simulations of boundary layer clouds passing over Graciosa Island.

Significant progress in the process-scale understanding of aerosol-cloud interactions, facilitated by observational data from 75 Graciosa Island, reveals that the seasonal cycle plays a significant role in aerosol activation. During winter, when the clouds are more decoupled and connected to stronger updrafts compared to summertime conditions (Wang et al., 2022; Zheng et al., 2022a), a higher fraction of accumulation mode particles tends to be activated ~~thereby resulting in decreasing the seasonal cycle in cloud droplet number concentration.~~ Despite higher activated aerosol fractions in winter, droplet number concentrations are lower due to less available aerosol compared to summer conditions (Wang et al., 2022). Large eddy simulations (LES) using 80 the WRF model with spectral bin microphysics and dynamical downscaling from a 19 km horizontal resolution to a 300 m grid spacing (Wang et al., 2020) demonstrated that imposing aerosol plumes at observed aircraft heights significantly reduces the effective droplet radius ( $ACI_r = \frac{\partial \ln(r_e)}{\partial \ln(N_{CCN})} \approx -0.11$ )  $ACI_r = \frac{\partial \ln(R_e)}{\partial \ln(N_{CCN})} \approx -0.11$  and increases the liquid water path ( $ACI_l \approx +0.14$ ). These cloud microphysical changes may modify the dynamics in the planetary boundary layer differently between seasons. Consequently, our work focuses on characterizing the cloud fraction response from numerous summer and 85 winter case studies provided by ACE-ENA, conducting ~~a deep-an in depth~~ a deep-an in depth investigation into mesoscale structural changes in clouds, and bridging the gap between cloud morphological changes and aerosol radiative forcing in low clouds.

### 2.1 Ground-based observations from ENA

Rain rate is retrieved ~~from-using~~ from-using a laser optical OTT Particle Size and Velocity (PARSIVEL-2) disdrometer, which measures the instantaneous rainfall rate ~~of-by quantifying the~~ of-by quantifying the water flux from ~~the-number-of~~ the-number-of drops in 32 size bins (0 to 25 mm) and 32

90 fall velocity bins (0.2 to 20 m/s) falling to the surface. The ~~rain~~-retrieval has a 6% absolute bias with respect to reference gauges over a 1-min sampling interval (Tokay et al., 2014) as provided in the LDQUANTS value added product (Hardin et al., 2020).

Cloud top height and low-level cloud fraction are estimated from the active remote sensing of clouds (ARSCL) product (O'Connor et al., 2004; Kollias et al., 2016; Clothiaux et al., 2001), which combines vertically pointing Ka-band radar and lidar data to produce high-resolution time-height cross sections of cloud boundaries.

95 Bottom of atmosphere shortwave and longwave radiative fluxes are provided by the ARM best-estimate cloud radiation dataset (ARMBECLDRAD; Xie et al., 2010; Tang and Xie, 2020) in hourly intervals using measurements from an infrared radiation station. Temperature and specific humidity profiles containing 266 altitude levels are provided every minute by the Interpolated Sounding (INTERPSONDE; Troyan, 2013) product that combines observations from radiosondes, the microwave radiometer (MWR), and surface meteorological instruments.

100 The effective radius of cloud droplets and optical depth in single-layer overcast liquid-only clouds is determined using the multifilter rotating shadowband radiometer (MFRSR) at a wavelength of 415 nm (Turner et al., 2021). The retrieval process relies on the algorithm developed by Min and Harrison (1996) for atmospheric radiative transfer. If the MWR successfully retrieves liquid water path, then the effective radius is calculated based on the MWR and MFRSR data. However, if ~~such~~ this information is not available we exclude it (occurring less than 30% of cases) from the analysis to ~~so that the results~~ remain sensitive to variations in aerosol concentration as shown in Christensen et al. (2023) avoid using fixed effective radius replacement values of 8  $\mu\text{m}$  in the ARM product.

## 2.2 ACE ENA Flights

The ARM Aerial Facility Gulfstream-159 (G-1) research aircraft flew from Terceira Island in the Azores during two intensive operational periods (IOPs) that occurred from June to July, 2017 and January to February, 2018 during ACE-ENA.

110 Deployments during both seasons are used to evaluate the vertical profile of the bulk liquid water content measured by the multi-element water content system (WCM-2000; Matthews and Mei, 2017). The multi-element water content measuring system utilizes a scoop-shaped sensor to measure total water content, capturing both liquid and ice phase hydrometeors. It incorporates two heated wire elements (021-wire and 083-wire), exposed directly to the airstream, along with a reference element exposed to the airflow but not to condensed water. Following the approach of Miller et al. (2022), we adopt the

115 WCM-2000 system due to its favorable agreement in liquid water content measurements compared to the Fast Cloud Droplet Probe and Two-Dimensional Stereo particle imaging probe measurement systems. The condensation particle counter (CPC) measures the number concentration of aerosols from 10 nm to 3 microns under-kinetic mode. Aerosol concentration uncertainties are approximately 15% (Fan and Pekour, 2018). The cloud condensation nuclei concentration is obtained from the CCN-200 particle counter aboard the G-1 aircraft providing CCN at approximately 0.2% supersaturation every second

120 (i.e., N\_CCN\_1 as discussed in Uin and Mei, 2019). To compare aerosol properties in clear-sky conditions with the WRF model, we select aircraft samples within a  $1^\circ \times 1^\circ$  region centered around the ARM site at 13:00 UTC  $\pm$  1.5 hr and below 2 km altitude, excluding those with cloud water content.

### 2.3 Satellite observations

Cloud-top effective droplet radius ( $R_e$ ) and cloud optical thickness ( $\tau_c$ ) are retrieved from the 1.6, 2.1, and 3.7- $\mu\text{m}$  channels; cloud top temperature, pressure, and height are retrieved from longer-wavelength thermal channels on the Moderate Resolution Imaging Spectroradiometer (MODIS) instrument. These data ~~are provided by~~, retrieved from the collection 6.1 cloud product (Platnick et al., 2017) ~~at~~, are at a 1-km pixel-scale resolution at nadir from satellites Terra and Aqua, ~~which pass~~ passing over the region at approximately 10:30 am and 1:30 pm local time, respectively. Of the three spectral channels used for  $R_e$  retrievals, the sensitivity of the 3.7- $\mu\text{m}$  channel is weighted closest to the cloud top, primarily due to the relatively strong absorption of water vapor at this wavelength (Platnick, 2000). Because errors in the adiabatic droplet number concentrations using the 3.7- $\mu\text{m}$  channel are considerably smaller than in the other bands (Grosvenor et al., 2018), we choose to use it for this study.

Imagery from the Geostationary Operational Environmental Satellite (GOES) Advanced Baseline Imager (ABI) of the National Oceanic and Atmospheric Administration (NOAA) GOES-R series satellite ~~Pinker et al. (2022)~~ (Pinker et al., 2022) is utilized to aid in visualizing the evolving characteristics of mesoscale cloud structures along Lagrangian trajectories. Full-disk images covering the entire region are made available every 15 minutes. These images have spatial resolutions of 0.5 km at nadir for the 0.64- $\mu\text{m}$  visible channel and 2 km for the 3.9- $\mu\text{m}$  and 11- $\mu\text{m}$  channels.

The Clouds and the Earth's Radiant Energy System (CERES) Synoptic (SYN1deg-1Hour) edition 4.1 product (Rutan et al., 2015) provide similar cloud top retrievals to MODIS using similar algorithms (e.g. the MODIS collection 5 product) as well as top and bottom of atmosphere shortwave and longwave radiative fluxes that are gridded globally at  $1 \times 1^\circ$  every hour through combining multi-spectral retrievals from a network of 16 geostationary satellites as well as the CERES instruments on Terra, Aqua, and Suomi National Polar-orbiting Partnership.

### 3 Methodology

Figure 1 depicts a 4-step procedure used to initialize and run the Weather Research and Forecasting (WRF) version 4.2 model (Skamarock et al., 2021) in a Lagrangian framework. This technique uses an inner nest that moves through the WRF model (outer domain) at specified time-steps. First, the Hybrid Single-Particle Lagrangian Integrated Trajectory (HYSPLIT; Stein et al., 2015) version 5 model is used to calculate a 6-hour back and a 6-hour forward trajectory using the Modern-Era Retrospective analysis for Research and Applications, version 2 (MERRA-2; Gelaro et al., 2017) reanalysis meteorological data. Trajectories are calculated from the middle of the planetary boundary layer (determined in HYSPLIT). This height has been shown to be representative for tracking the general flow of boundary layer clouds over the ocean (Christensen et al., 2020; Kazil et al., 2021; Christensen et al., 2023). Back trajectories are initialized at the Graciosa Island ARM site at 10 am local time before the Terra (morning at 10:30 am) and Aqua (afternoon at 1:30 pm) MODIS overpass times. Forward and backward trajectories are initialized at Graciosa Island and run for 6-hours. These trajectories are combined to form a 12-hour trajectory starting from the tail of the back trajectory and ending at the tail of the forward trajectory. This method ensures that the airmass transits over the ARM site.

### 3.1 WRF Modeling

Nested simulations are performed using the WRF model (Figure 1 box 2). The outer (static) domain ~~size~~ is  $12^\circ \times 12^\circ$  and is centered over the ARM site on Graciosa Island. The region is large enough to span the entire length of the back and forward Lagrangian trajectories. The outer domain has a horizontal grid spacing of 4 km and a vertical grid that is log-stretched where  
160 the spacing is approximately 50 m near the surface and increases to 150 m throughout the PBL to the top of the model at 20 km. The model time-step is 10 s. The outer domain is used to characterize the large-scale meteorological flow and boundary conditions for the inner domain.

The inner domain allows for convection-permitting scales and moves along the HYSPLIT trajectory using the multi-incremental 4D-Var system which allows for translating (moving) nests within WRF (similar to vortex tracking for hurricanes  
165 as described in Zhang et al., 2014). WRF was compiled using preset moves to permit higher spatial resolution simulations within the inner domain which is computationally more efficient than high resolution across the entire outer domain. The inner domain translates in time (across the outer domain) according to the pre-computed locations using HYSPLIT. Given the spatial scales of typical cellular maritime cloud organization (30 to 40 km; Wood, 2005), the inner domain is spatially large enough to capture the largest scales of variability spanning approximately  $200 \times 300 \text{ km}^2$  with a horizontal grid-spacing that  
170 is 5 times finer than the outer nest (800 m) with the same vertical resolution.

Boundary conditions are initialized and updated every 6 hours during simulation using reanalysis data from MERRA-2 which is spatially gridded at 0.5-degree resolution with 72 vertical levels and provided every 6 hours. We have tested WRF using other meteorological data sets (~~details described in see~~ [Text S1](#) and [Fig. S1](#) for details) and find that the choice of the reanalysis product does not significantly alter the results. To coincide with earlier work (Christensen et al., 2023) we use  
175 MERRA-2 to drive the WRF boundary conditions for this study.

We use a 6-hour spin-up period to allow sufficient time for the cloud properties to reach steady state. After this period, the inner two-way nest begins to move within the WRF model according to the HYSPLIT trajectory computed using the same reanalysis product as that was used to drive the WRF model. The simulations are performed with the aerosol-aware Thompson bulk microphysical parameterization scheme (Thompson and Eidhammer, 2014) with explicit cloud droplet nucleation treat-  
180 ment following Köhler activation theory. Look up tables generated from parcel modeling are used to provide the cloud droplet number concentration based on predicted temperature, vertical velocity, number of hygroscopic aerosol particles also referred to as ‘number of water friendly aerosols’ (NWFA), and predetermined values of hygroscopicity parameter and aerosol mean radius. Aerosol sensitivity experiments follow the same approach as described in Thompson and Eidhammer (2014) in which the input mass mixing ratio of each aerosol species (dust, sea salt, black and organic carbon, and sulfate aerosols) is obtained  
185 from GOCART and is converted to NWFA concentration using assumed lognormal distributions with characteristic diameters and geometric standard deviations taken from Chin et al. (2002) (their Table 2). Next, we modify the NWFA concentration profile climatology averaged over 7 years using the following scale factors: 0.01 (pristine), 0.1 (clean), 1.0 (control), and 10.0 (polluted) for each experiment, respectively (Figure 1 box 3). Note, that no changes are made to the assumed aerosol chemical species composition, hygroscopicity parameter (0.4 in experiments performed in this research), and aerosol mean radius (0.04

190  $\mu\text{m}$ ). These scale factors significantly affect the NWFA concentration as shown in Figure S2. Lower condensation particle concentrations (CPC) in cloud-free air sampled by the aircraft suggest that the control simulation of NWFA may be more polluted than the observations on this particular day and across seasons (Figure S3). However, the CPC and NWFA ~~serve~~ serve as a rough comparison as the characteristics (namely the size distribution and hygroscopicity) of these two quantities may differ. As discussed later, cloud droplet number concentrations are also affected by NWFA with median values broadly approaching  
195 20, 50, 250, and  $450\text{ cm}^{-3}$  for our pristine (N1), clean (N2), control (N3), and polluted (N4) aerosol experiments, respectively.

The Level-3 Mellor-Yamada-Nakanishi-Niino (MYNN3) PBL scheme (Nakanishi and Niino, 2009) predicts TKE and other second-order moments within the PBL. The Rapid Radiative Transfer Model for GCMs (RRTMG) specifies the size of hydrometers and utilizes the correlated-k approach to calculate fluxes and heating rates accurately (Iacono et al., 2008) and efficiently through its use of a Monte-Carlo Independent Column Approximation technique (Pincus et al., 2003). The simulations utilize  
200 the Noah land surface model (Barlage et al., 2010) as well as the Tiedtke cumulus scheme (Zhang et al., 2011).

Model evaluation (Figure 1 box 4) is carried out using output from the WRF-Solar model (Jimenez et al., 2016) ~~which, when run online, passes the the~~ which passes the effective radius of cloud particles from ~~microphysics to radiation parameterizations (Thompson and Eidhammer, 2014)~~ thereby affecting the microphysics to the radiation parameterization scheme (Thompson and Eidhammer, 2014), impacting cloud albedo and ~~permitting the enabling~~ quantification of the aerosol indirect effect (Thompson et al., 2016). WRF-  
205 Solar includes a solar diagnostics package that ~~adds a number of outputs several~~ two-dimensional variables ~~output from which we use, including~~ cloud fraction, liquid effective droplet radius, optical thickness, and liquid water path ~~(computed from the effective radius and optical thickness quantities, i.e.,  $LWP = \frac{2}{3}\tau_c R_e$  where  $\tau_c$  is the cloud optical thickness, and  $R_e$  is the effective droplet radius (Stephens, 1978))~~. These quantities (that are weighted towards the cloud top) have been shown to be comparable with MODIS observations (Otkin and Greenwald, 2008). A summary of the  
210 model setup is listed in Table 1.

### 3.2 Case Studies

Figure 2 shows our selected case studies. Days are selected based on the following criteria: 1) a dearth of high-level cloud over the trajectory for optimal comparison with satellite retrievals, 2) aircraft measurements coinciding with intensive operation periods (IOP) 1 (6/25/2017 - 7/25/2017) and 2 (2/1/2018 - 2/25/2018), and 3) diverse meteorological conditions to study  
215 the impacts of precipitation, atmospheric stability, and ~~free-tropospheric~~ free tropospheric humidity states on aerosol-cloud interactions. Across the experiments, the height of the PBL top varied from 600 m to 1710 m and the surface air temperature varied from  $13 - 22^\circ\text{C}$  as determined by meteorological soundings averaged over the entire day. Daily total accumulated precipitation from the disdrometer varied from 0 - 4 mm. A wide range of cloud patterns were observed including disorganized (small, isolated clouds or clouds with no discernible pattern), homogeneous (solid cloud deck with no discernible pattern),  
220 closed-cells (cells filled with cloud), open-cells (cells where the center is devoid of cloud). These classifications are broadly inferred using the definitions described in ~~(Wood and Hartmann, 2006)~~ Wood and Hartmann (2006). Table 2 lists key quantities of interest for the cases displayed in Figure 2. It is noteworthy to mention that while we aim to select cases which did not have ice cloud in the observations, the WRF model sometimes simulated them above the boundary layer (7/18/17) and within the

boundary layer during two of the wintertime IOP case studies (1/24/18 and 1/25/18). Potential impacts of simulated ice cloud  
225 on the analysis are discussed in subsequent sections.

### 3.3 Lagrangian Framework and Dataset Integration

Figure 3 shows the evolution of shallow clouds in the Lagrangian trajectory for the lightly drizzling day of 7/18/2017. This  
case study forms the backbone for many of the inter-comparisons made throughout this work [due to the distinct closed cell  
features and persistence of the stratocumulus cloud deck throughout the day](#). Satellite retrievals from GOES and MODIS are  
230 aggregated over a  $1 \times 1^\circ$  region (yellow box) during each time-interval (15 minutes) along the trajectory. CERES gridded-data  
is interpolated in space and time to the same trajectory grid-box. WRF simulations at roughly km-scale are aggregated over  
the same region and timescale as the Lagrangian trajectory. Both the observations and simulations show persistent closed cell  
clouds throughout the day. These clouds produce very light drizzle as indicated by the Ka-band radar (Fig. 2e) and disdrom-  
eter measurements at Graciosa Island (Table 2). An evident wake island effect is observed and simulated in the downstream  
235 region from the Azores. In general, the low-level flow and horizontal displacements of the clouds are well captured using the  
Lagrangian framework as depicted in Movie S1.

## 4 Results

In the first part of the analysis we quantify the effect of aerosol changes on the mesoscale structure of clouds (i.e. size and  
distance between cloud cells) and associated radiative impacts from an ensemble of 40 WRF simulations spanning 10 different  
240 case studies with 4 varying aerosol concentrations (a set of 4, for each case study day) offering diverse meteorology and  
cloud types. This particular set of simulations uses MYNN3 and Thompson (aerosol-aware) PBL and microphysics schemes,  
respectively. In the second part [\(section 4.3.2\), we assess and quantify](#) variations in the aerosol indirect effect [from-on](#) case  
study day 7/18 [using-by-employing](#) different PBL and microphysical scheme choices across 26 WRF experiments [is-assessed  
and-quantified](#).

### 245 4.1 Impact of aerosol on the mesoscale structure of clouds

Cloud objects are detected using [the-a](#) watershed technique, following the methodology described in Wu and Ovchinnikov  
(2022). Because the standard WRF model output does not include simulated channel reflectances for MODIS, comparisons are  
made based on the *LWP*. The only difference between Wu and Ovchinnikov (2022) and our study is that we use *LWP* instead  
of the MODIS reflectance. As *LWP* scales well with the visible cloud albedo (Stephens, 1978), the replacement of *LWP* for  
250 visible reflectance is suitable after thresholds have been linearly scaled. Moments of the *LWP* distributions have been used for  
cloud classification of marine stratocumulus in several studies (e.g., see Wood and Hartmann, 2006; Zheng et al., 2018). The  
segmentation procedure initially smooths the *LWP* field to remove random field variations while preserving object boundaries  
using a two-dimensional Gaussian filter with a kernel standard deviation of  $250 \text{ g m}^{-2}$ . Next, cloud objects are detected using a  
watershed technique. A centroid is assigned to each cloud object based on the distribution of cloudy pixels with *LWP* greater



255 than  $100 \text{ g m}^{-2}$ . Cloud objects are formed if a common interface is shared. An edge weight is computed, and if the ~~difference between adjacent pixels is greater~~ area-weighted mean difference between pixels along the interface is smaller than  $4 \text{ g m}^{-2}$  the two objects are merged and a new centroid is assigned to the object.

To determine the spacing between cloudy object centers, we compute the distance of each cloud object centroid to all other centroids and select the minimum distance (i.e.,  $D_c$ ). Due to variable sizes of the cloud objects, we also compute the distance  
260 of all edge pixels of an object to all of the edge pixels of all other objects and select the minimum distance ( $D_e$ ). This latter method provides an estimate of the closest distance between neighboring cloud object boundaries, thus removing the effect of cloud fraction on distances between clouds that is not accounted for with cloud object centroids.

Cloud objects are identified in WRF (Fig. 4b) every 15 mins along the trajectory and in MODIS at the Terra and Aqua overpass times (Fig. 4d). Cloud area ranges from about  $1 - 500 \text{ km}^2$  in WRF and MODIS (Fig. ~~S3a~~S4a). The majority are  
265 at scales less than about 10 km, a result similarly found in Wu and Ovchinnikov (2022) and (~~Wood and Hartmann, 2006~~) Wood and Hartmann (2006), based on power spectral analysis of the spatial variance in *LWP*. The distance between cloud object centroids is similar between MODIS and WRF with a mean value of approximately ~~11~~12.1 km and median value of roughly ~~5~~10.7 km for this particular case study (Fig. ~~S3b~~S4b).

The size and spacing between cloud objects is to some extent dictated by the background aerosol concentration. Figure 5a and  
270 b ~~shows~~show that the average cell area and spacing between object centroids increases as the background aerosol concentration increases. The distance between cloud edges decreases as the aerosol concentration increases (Figure 5c). This is evident when comparing ‘snapshots’ of the pristine and polluted experiments taken at the same time (Fig. 5d-e). The cloud objects are spreading away from each other but they are also becoming larger and filling the gaps between clouds as aerosol loading increases. Similar behavior is found on 7/15/2017 (as depicted in Fig. S5) and generally across all case studies (discussed in section 4.3).

To characterize uncertainty and determine whether this relationship is robust, a sensitivity test of the segmentation algorithm is performed over a range of minimum *LWP* thresholds for defining cloud object edges spanning  $1$  to  $500 \text{ g m}^{-2}$ . Figure  
280 ~~S4~~S6 shows that the area of the cloud objects become larger with increasing aerosol concentration. This response is robust across the full range of *LWP* threshold values. The largest sensitivity of this relationship occurs around  $200 \text{ g m}^{-2}$ . This unique threshold *LWP* value is also a turning point for which further increases in *LWP* decrease the number of detected cloud objects, which impacts cell separation distance. Furthermore, the cloud fraction is larger under polluted conditions and this relationship is robust for each minimum *LWP* threshold value (Fig. ~~S4d~~S6d). As  $100 \text{ g m}^{-2}$  forms roughly the midpoint value we select this representative threshold for segmenting clouds in this analysis.

## 4.2 Aerosol-cloud interactions

285 Two case studies, one with lightly precipitating clouds and another with heavier precipitating clouds are examined in detail during the summertime IOP period for quantifying the effects of aerosol on precipitating and lightly-precipitating clouds.

### 4.2.1 Lightly-Precipitating clouds

On 7/18/17 closed-cell type clouds were found in the vicinity of the Azores. The clouds produced a light amount of precipitation where only approximately 0.02 mm was recorded in the distrometer measurements from ARM. Aircraft measurements of the cloud water content on this day fit within the range of variability simulated for clouds in the WRF model (Figure 6a). Cloud tops from the aircraft measurements imply that ~~the~~ WRF simulates a slightly deeper than observed boundary layer by approximately 200 m. We find reasonable agreement between MODIS, CERES, and ARM data sets with the WRF simulations (Fig. 7). Cloud optical depth and radiative fluxes tend to agree more closely with the clean and control WRF experiments. The agreement not being closest with the control experiment may be indicative of the following issues: 1) a bias in the climatological aerosol concentrations (being too high), 2) the Thompson scheme may be nucleating too many aerosols, or 3) scavenging rates are not large enough. Despite these differences, the chosen schemes resolve essential characteristics of a realistic boundary layer based on the reasonable agreement in the cloud relevant properties.

Rain water mixing ratio, also forming closer to cloud top in the cleaner experiments, decreases up to an order of magnitude as background aerosol concentration increases (Figure 6b). A modest increase in cloud water content and cloud water mixing ratio is found in the more polluted simulations throughout all levels in the cloud. This result is consistent with the indirect effect using the Thompson microphysics scheme described in Thompson and Eidhammer (2014). An increase in aerosol concentration also results in smaller cloud droplet effective radius (Fig. 7a), larger cloud optical thickness, larger liquid water path, and larger droplet concentration (Fig. 7b,c,d); cloud-top quantities are obtained from WRF-Solar. The more polluted aerosol experiments with optically thicker clouds result in more reflected solar radiation at the top of the atmosphere and less incoming solar radiation at the bottom of the atmosphere despite having slightly lower cloud tops. The slightly elevated cloud tops in the more pristine simulation also have elevated cloud bases and are more decoupled from surface moisture. Nonetheless, all simulated cloud top heights are within the range of variability in the ARM and satellite observations.

Cloud properties tend to vary over the course of the trajectory with increasing cloud optical thickness, liquid water path, and cloud top height. This is accompanied by an increase in sea surface temperature and more unstable boundary layer conditions along with rising lifted condensation level and decreasing free tropospheric humidity (Fig. ~~S5S7~~). A deepening boundary layer is expected given the warming sea surface temperature (Eastman et al., 2016) but despite the changing meteorological conditions over the trajectories, the cloud ~~changes-related alterations attributed~~ to changes in aerosol loading ~~are systematic along the trajectories for a 12-hour~~ remain systematic throughout the 12-hour period.

### 4.2.2 Precipitating clouds

In comparison to the previous case study, the boundary layer on 7/15 is about 750 m deeper and the accumulated rainfall is significantly larger; 3.9 mm. Much like the previous light drizzle case study, the properties of precipitating clouds on 7/15/17 also broadly fit within the range of variability in cloud water content as measured by aircraft observations (Figure 8) and LWP by satellite and ARM retrievals (Fig. ~~S6S8c~~). Simulated cloud top ~~heights tend~~ height tends to be higher than the observations during the afternoon hours. Figure 2d ~~shows that the clouds were much more vigorous as indicative by the~~ reveals more

320 ~~vigorous clouds, as indicated by~~ relatively large radar reflectivities ~~in the during~~ early morning and late afternoon periods  
outside ~~of the trajectory period which could be responsible for the mismatch in the~~ the trajectory timeframe. ~~This difference~~  
~~could contribute to the observed mismatch between~~ simulated and actual cloud top heights. ~~Nevertheless, peak cloud water~~  
~~contents~~ ~~Despite this,~~ in the control simulation ~~are about,~~ peak cloud water contents are approximately 40% larger ~~and peak~~  
325 ~~rain water, and peak rainwater~~ mixing ratios are about 90% larger on 7/15 (precipitating case study) compared to 7/18 (drizzling  
case study). Furthermore, the cloud water content increase due to increasing aerosol concentration is significantly larger on  
7/15 compared to 7/18.

Simulations with elevated concentrations of aerosols have larger cloud top shortwave and longwave radiative cooling rates.  
The net radiative cooling rate decreases from approximately -10 K/d in the clean simulations to -30 K/d in the more polluted  
simulations (Figure 9). Mean vertical and horizontal wind velocity near the cloud top also tends to be larger in the more polluted  
330 simulations. Vertical velocity variance and turbulence throughout the boundary layer tend to be larger in the more polluted  
simulations. Vertical profile shapes of these quantities are similar, albeit less ~~in magnitude, for the light drizzle simulations.~~  
~~Rainfall suppression pronounced, on 7/18 (Figure S9).~~ Stronger updrafts in the more polluted simulations ~~make the updrafts~~  
~~weaker in the lower planetary boundary layer but stronger in the upper PBL~~ where radiative cooling rates are larger ~~. As a~~  
~~result, polluted clouds exhibit~~ coincide with larger lateral displacements near the base of the inversion ~~causing and may be~~  
335 partially responsible for causing the significant widening of the clouds and ~~increase in~~ increased cloud fraction.

Additional tests are carried out at 1 km horizontal grid spacing to determine the relative roles of cooling caused by rain  
drop evaporation (by setting the temperature and moisture tendencies caused by changes in rain mass evaporation in the  
Thompson microphysics scheme to zero), cloud radiative effect (setting icloud=0 in the namelist file), and the cumulus scheme  
(by turning it off) on the results. Rain evaporation below cloud base stabilizes the atmosphere, producing decoupling and  
340 less turbulence (Wood, 2012). However, ~~Fig. S7~~ Figure S10 shows that turning off rain droplet evaporation results in only a  
small relative change in cloud and rain mixing ratios, radiative cooling, and turbulence. Turning off the radiation to the clouds  
significantly decreases turbulent mixing, cloud top height, and rain water mixing ratio. Similarly, turning off the cumulus  
scheme significantly decreases cloud and rain water mixing ratio and radiative cooling rates.

~~Fig. S8 shows the outcome of these~~ Figure S11 illustrates the impact of sensitivity experiments on ~~the aerosol impact aerosol~~  
345 effects on cloud properties. In general, an increase in aerosol concentration enhances cloud fraction, liquid water path, and  
cloud area extent as aerosol loading increases. Turning off cloud interactions with radiation removes the effects of changes in  
cloud radiative heating and cooling, but clouds still expand (albeit less so) simply due to precipitation suppression by aerosols.  
This may indicate that low-clouds expand due to precipitation suppression, through reducing the magnitude of the primary  
cloud sink; next changes in radiative effects cause further increases in cloud fraction (approximately 100% more based on  
350 Fig. ~~S8~~ S11). This cloud radiative feedback suggests an important contribution to promoting the initial cloud expansion via  
precipitation suppression by aerosol. For removal of rain evaporation, the precipitation effect on PBL turbulence is turned off.  
While this no longer conserves energy (which is unavoidable in such sensitivity tests) we continue to simulate strong cloud  
expansion due to increased aerosol concentration and this is largely due to the suppression of precipitation and growth of the  
cloud.

### 355 4.3 Aerosol-cloud interactions across 10 case studies

A suite of aerosol experiments spanning 10 case studies with varying meteorological conditions provides 40 WRF simulation experiments to examine aerosol indirect radiative effect across a range of meteorological and cloud conditions. These case studies are summarized in Table 2.

#### 4.3.1 Aerosol indirect radiative effect

360 The aerosol indirect radiative effect is calculated from the change in the top of atmosphere outgoing shortwave radiative flux caused by a change in  $N_d$  and can be written as

$$RE_{aci} = -\overline{F^\downarrow} \phi_{atm} \frac{f_c \alpha_c (1 - \alpha_c)}{3N_d} \frac{f_c \alpha_c (1 - \alpha_c)}{3N_d} \left( 1 + \frac{5}{2} \frac{\Delta \ln L}{\Delta \ln N_d} + \frac{3(\alpha_c - \alpha_{clr})}{\alpha_c (1 - \alpha_c)} \frac{3(\alpha_c - \alpha_{sfc})}{\alpha_c (1 - \alpha_c)} \frac{\Delta \ln f_c}{\Delta \ln N_d} \right) \overline{\Delta N_d} \quad (1)$$

where,  $F^\downarrow$  is the top of atmosphere (TOA) incoming solar radiation,  $\phi_{atm}$  is the transfer function that accounts for the average albedo transmissivity (reflection and absorption) of the non-cloudy air above the surface and takes an average value of 0.7 (Diamond et al., 2020),  $f_c$  is the cloud cover fraction,  $\alpha_c$  is the cloud albedo,  $N_d$  is the droplet concentration,  $L$  is the liquid water path, and  $\alpha_{clr}$  is the clear-sky albedo,  $\alpha_{sfc}$  is the surface albedo. The full derivation, based on Quaas et al. (2008) and Christensen et al. (2023), is described in Text S1.

Quantities in equation 1 are computed over each hourly interval obtained in hourly intervals over a  $1^\circ \times 1^\circ$  domain moving along the trajectory. The  $\Delta$  symbols denote differences between aerosol experiments of varying aerosol concentrations (e.g. dirty-pristine, control-clean, etc.). There are six possible pairs which include, polluted – control  $\Delta(N4-N3)$ , polluted – clean  $\Delta(N4-N3)$ , polluted – pristine  $\Delta(N4-N1)$ , control – clean  $\Delta(N3-N2)$ , control – pristine  $\Delta(N3-N1)$ , and clean – pristine  $\Delta(N2-N1)$ .  $\overline{F^\downarrow}$  is the daily-mean solar insolation,  $\frac{f_c \alpha_c (1 - \alpha_c)}{3N_d}$  and  $\frac{3(\alpha_c - \alpha_{sfc})}{\alpha_c (1 - \alpha_c)}$  are computed from mean quantities of the paired aerosol experiments, and  $\overline{\Delta N_d}$  represents the difference between two aerosol experiments. A linear least squares method is also used to compute  $\frac{\Delta \ln L}{\Delta \ln N_d}$  and  $\frac{\Delta \ln f_c}{\Delta \ln N_d}$  terms. On average, we find that the difference in methods (difference between experiments vs using a fitted slope across all four experiments) varies by less than 15% mean difference in cloud droplet number concentration between paired aerosol experiments. By using a wide range of aerosol concentrations we capture the range of aim to capture variability in ACI but acknowledge that non-linearity in the relationship between cloud variables with  $N_d$  may be missed from the use of only 4 aerosol experiments.

Figure 10 shows the relationship of key variables as they change in response to increasing background aerosol concentrations in the WRF model. In most cases, there is good agreement in the sign of the response across diverse case studies. An increase in aerosol concentration enhances the top of atmosphere reflected sunlight, cloud fraction, liquid water path, cloud optical thickness, and cloud object area. A robust decrease in droplet effective radius is also evident. While responses are mostly consistent, the magnitude can vary substantially. Cases where significant precipitation occur (7/15 and 1/25) exhibit the largest increases in liquid water path, cloud optical thickness, and cloud object area. Days having light rain (7/18, 7/6, 7/12) or no measurable rain (6/30, 1/24) have significantly weaker responses by comparison. Figure 11a,b shows the effect of precipitation

on the liquid water path and cloud fraction aerosol adjustments. While there is some scatter across experiments, this result generally agrees with Chen et al. (2014); an increase in aerosol concentration has a stronger radiative effect on precipitating clouds compared to non-precipitating clouds due to the suppression of precipitation causing cloud water to increase. While drizzle suppression reduces scavenging of cloud droplets and goes into spreading the cloud vertically, the horizontal spreading of the clouds through increased cloud object area is highly significant.

The Twomey radiative effect is estimated as  $-13.7 \pm 11.0$   $\text{W m}^{-2}$  with a range extending from  $-17.6$  to  $-4.1$   $\text{W m}^{-2}$  across these case studies. This estimate is based on the local daily-mean solar insolation, which at this location, can vary significantly between winter and summer IOP periods. Note, this estimate is the radiative effect, not the radiative forcing, and hence does not include the changes in aerosol concentration attributed to anthropogenic sources (i.e. the present-day minus pre-industrial values). The radiative effect is estimated from 6 different aerosol experiment pairs (discussed above) that have a wide range of aerosol concentrations (as shown in Fig. S1-S2 and Fig. S3). The cloud properties and radiative effects associated with each case study are listed in Tables S1 – S10. The quantification of the modeled sensitivity in the cloud radiative effect to changes in cloud droplet concentration are similar to those found in Goren and Rosenfeld (2014) or from local-scale aerosol perturbations found in ship tracks (Christensen and Stephens, 2012) satellite observations of ship tracks (Christensen and Stephens, 2012; Goren and Rosenfeld, 2014).

To make the results more intuitive, Table 3 lists the ratios of the liquid water path and cloud fraction adjustments scaled by the Twomey effect. These enhancements range from 10 - 150 % for the  $LWP_{adj}$ ; a result that is similar to that found across multiple GCM experiments in (Gryspeerd et al., 2020) and the observations in Gryspeerd et al. (2020) and in the observations of Goren and Rosenfeld (2014). During both IOP periods we find that the largest indirect radiative effects tend to coincide with the largest daily precipitation rates (Figure 11c). These cases are also consistent with those which show the largest cell area growth as a function of aerosol loading (Figure 10).

The cloud object area expansion relationship is not as strong during the wintertime IOP period, possibly because ice is produced and can lead to glaciation indirect effects that can produce opposite precipitation responses compared to warm clouds (Lohmann, 2002; Christensen et al., 2014). Figure S9 shows that the fraction of liquid-to-ice is very high in the. Figure S12 reveals the presence of ice on 1/24/18 and 1/25/18 cases. Thus, while some ice is simulated, the general tendencies for the Twomey, and intriguingly, the Twomey effect and rapid adjustments, as well as the cloud morphological changes, remain consistent with the warm cloud responses exhibit comparable agreement in these cases, as seen in the warm cloud case study days (Figure 10). While aerosol effects on ice clouds are a key component to quantifying aerosol radiative forcing, it remains outside the scope of this study to examine it further in this work. Although the Thompson microphysics scheme considers ice multiplication from rime-splinters through the Hallett–Mossop process (Hallett and Mossop, 1974), a phenomenon known to lead to cloud morphology breakup and alteration, accompanied by enhanced precipitation (Abel et al., 2017; Eirund et al., 2019), we haven't altered ice-friendly nuclei concentrations in this study. Modifying such concentrations could offer additional insights into aerosol-ice cloud interactions in future research.

### 4.3.2 Impact of changing PBL and microphysics schemes

420 We devise a set of sensitivity experiments where the microphysics and PBL schemes are varied to assess the uncertainty of modeling boundary layer clouds and ACI. These simulations use the double-moment Morrison microphysics (Morrison et al., 2005) scheme with fixed cloud droplet number concentration. For the Morrison scheme, we used fixed droplet number concentrations with values of 20, 80, 320, and 1020  $\text{cm}^{-3}$  for our pristine (N1), clean (N2), control (N3), and polluted (N4) aerosol experiments, respectively. Values for the more polluted runs were increased to coincide with the scale factors used in  
425 the Thompson (aerosol-aware) scheme for simulating similar values of the cloud droplet number concentrations. The additional PBL schemes for testing use the non-local Yonsei University (YSU; Hong et al., 2006) or local Mellor–Yamada–Janjic (MYJ; Mellor and Yamada, 1982) closure flux models. These schemes have differences in vertical mixing strength which affect entrainment of dry air from above the PBL and can impact cloud properties differently depending on the scheme chosen (Hu et al., 2010). A summary of each sensitivity experiment is listed in Table 4. Note, running the Morrison microphysics  
430 scheme with fixed droplet number concentration does not allow for a full positive aerosol-cloud-precipitation feedback cycle as simulated in some LES simulations (e.g., Yamaguchi et al., 2017). This has been shown to have a significant influence on the mesoscale structure of clouds, and hence, cloud fraction (Goren et al., 2019; Diamond et al., 2022), potentially having a significant impact on the net radiative effect in this sensitivity study.

Figure 12 shows a comparison of WRF simulated  $LWP$  with satellite observations from several different microphysics  
435 and PBL schemes for the 7/18/2017 case study described in Figure 3. All schemes simulate boundary layer cloud in a similar geographic region as that observed by satellites. However, some of the WRF schemes under-predict  $LWP$  and cloud top heights, in particular the YSU and MYJ PBL schemes (as shown in Fig. S10-S13) with respect to MODIS. The MYJ scheme tends to produce smaller cloud cells containing much smaller liquid water paths compared to the YSU and MYNN3 schemes. In general, most of the simulations reproduce the vertical profiles of temperature, humidity, wind speed, and wind direction  
440 compared to ARM radiosonde measurements (Fig. S11-S14) but with a slightly elevated capping inversion and dew point temperature. Overall, we find the best agreement with the Thompson and MYNN3 PBL schemes regarding how close the cloud and atmospheric state compare to the observations.

To test the impact of using different schemes in WRF on the aerosol indirect effect, four aerosol experiments are carried out for each model configuration, yielding a total of 24 simulations to quantify the range of variability in aerosol indirect effect for  
445 the case study occurring on 7/18/17. Due to computational constraints, we ran these simulations at a lower spatial resolution (3 km grid spacing for the inner nest) using 99 vertical levels. Here we exclude cloud area changes in the analysis due to the poorer ability of the model to simulate these structures at lower resolution and focus more on the microphysical changes across these model configurations instead.

Figure S12-S15 shows the aerosol perturbations of various cloud properties for each of the six WRF configurations. Like  
450 before, all simulations show that an increase in aerosol concentration results in an increase in the reflected solar radiation, a reduction in cloud droplet effective radius, and an increase in cloud optical depth. The lower simulation resolutions produce similar sensitivities compared to the higher resolution simulation runs. For example,  $\Delta \ln \tau_c / \Delta N_a \sim \Delta \ln N_d$  for the higher res-

olution run is  $0.55 \pm 0.12$  and  $0.48 \pm 0.15$  for the lower resolution run. It is noteworthy that the liquid water path and cloud thickness responses are negative in some of the configurations; however, a t-test indicates that there is not a significant difference from zero. The variations ( $\sigma RE_{aci} = \frac{\sigma_{err}}{RE_{aci}}$ , estimated from the standard error,  $\sigma_{err}$ , computed from the standard deviation normalized by the square root of the 10 cases divided by the total indirect effect effect) across experiments is approximately  $\pm 30\%$ . Given this range of variability in the indirect effect, we infer the microphysical cloud responses are robust across a wide range of possible model configurations. Thus, variations larger than this level in analyses of the 10 case studies with the Thompson and MYNN schemes are likely to be more related to meteorological and cloud state modulations as opposed to these particular chosen WRF schemes.

## 5 Conclusions

We devised a series of realistic WRF simulations using boundary conditions from MERRA-2 reanalysis to simulate PBL clouds as they pass over Graciosa Island in the Azores during the ACE-ENA field campaign. Kilometer-scale simulations were carried out within an inner-nest that moves along the Lagrangian flow of the PBL, making higher resolution simulations computationally feasible for studying aerosol-cloud interactions. The Lagrangian framework allows for the analysis of an evolving cloud field over time, although, for relatively short-timescales like those used here the aerosol responses were roughly consistent along the length of trajectories. Cloud water content, temperature, humidity, and wind profiles were in the range of acceptable uncertainty as determined by comparison with aircraft observations and radiosonde measurements from Graciosa Island. WRF-simulated cloud microphysical properties and radiative fluxes were generally in closer agreement to the clean (not control) experiments. This result suggests that the baseline NWFA concentration are biased high at Graciosa Island. With the exception of WRF simulating higher cloud tops during the afternoon compared to MODIS and ARM, the simulated cloud and radiative properties in general tend to fit within the range of observed uncertainty.

With these simulations, we addressed the following research questions:

- **To what extent does a change in aerosol concentration modify the area and spacing between cloud cells?** An increase in aerosol concentration suppresses precipitation, causing liquid water content and liquid water path to increase throughout the PBL. Through applying the cloud segmentation watershed algorithm developed by Wu and Ovchinnikov (2022) we find that cloud water mass is re-distributed through the PBL horizontally and in some cases vertically through the expansion of the clouds. This is accompanied by a decrease in clear skies between clouds. The suppression of drizzle through an increase in aerosol concentration results in more cloud water. The cloud top radiative cooling rates and turbulent eddies are increased in strength under polluted conditions. Larger vertical velocity variance and horizontal winds near the cloud tops was typically found in the simulations with more aerosol. Through this process, the additional water (not lost through drizzle) in polluted clouds is re-distributed both vertically as well as horizontally. This results in the expansion of cloud cells.
- **How does the aerosol indirect radiative effect vary over diverse meteorological conditions?** The sign of the aerosol indirect radiative effect is robust across all case study days. They all exhibit liquid water path and cloud fraction increases

with increasing aerosol concentration, a similar result also found in the WRF simulations of Zheng et al. (2022a). As found in previous studies (e.g., Chen et al., 2014), the strength of the radiative effect is strongly tied to the occurrence of precipitation. We find that the cloud area expansion is greater in environments that support deeper boundary layers with heavier precipitation and the magnitude is generally smaller in case studies with less background precipitation.

490 – **How does changing PBL and microphysics schemes affect the aerosol indirect effect?** A set of six WRF configurations using three different PBL and two different microphysics schemes revealed robust cloud responses to changes in aerosol concentration. The range of variability on total indirect effect across configurations was approximately 30%. We conclude that the choice of valid WRF schemes plays less of a role on the indirect effect (at least from these configurations for one case study) than the impact of precipitation on aerosol-cloud interactions where the variations are larger  
495 across the 10 case studies.

– **How do liquid water path and cloud fraction adjustments compare to the Twomey effect?** Aerosol radiative effects were decomposed into contributions from the Twomey effect and liquid water path and cloud fraction adjustments. The liquid water path and cloud fraction adjustments scale as 74% and 51% increases relative to the Twomey effect, respectively. These adjustments are ~~larger than those found in prior observations (Goren and Rosenfeld, 2014) especially in the simulations where the daily mean precipitation is~~ largest where an increase in aerosol can have a larger impact on drizzle suppression and cloud water path enhancement. Our simulation estimates of the scaled adjustments are larger but within the range of uncertainty estimated from satellite observations (Goren and Rosenfeld, 2014).  
500

In all 10 case studies, LWP adjustments were ~~consistently~~ positive. This result remained consistent even when different PBL and microphysics schemes were employed. Despite the diversity in meteorological conditions, we were unable to simulate  
505 the negative LWP responses sometimes reported in LES studies, albeit using different boundary conditions (Ackerman et al., 2004; Seifert et al., 2015). Negative LWP responses have been documented in satellite observations of ship tracks (Christensen and Stephens, 2012), downstream from volcanic aerosol emissions (Malavelle et al., 2017; Toll et al., 2017), and more broadly in non-precipitating clouds, particularly in the presence of excessive dry air conditions above the marine boundary layer (Chen et al., 2014). Our findings generally align with positive LWP responses. ~~These are~~ also identified in WRF LES  
510 simulations from the same region used in Wang et al. (2020). ~~However, the lack~~ Although, the absence of a negative LWP response in our study may be attributed to ~~an underestimation of autoconversion, a variety of processes. First, uncertainties in the autoconversion rate~~ (a tunable parameter that ~~delays the formation of raindrops, resulting in the increase in LWP as  $N_d$  increases. Similarly, underestimating~~ affects the formation rate of raindrops) may lead to a positive LWP response as droplet number concentrations increase if this rate is underestimated (Mülmenstädt et al., 2020; Christensen et al., 2023). Second, sedimentation and entrainment rates ~~may lead to a less efficient~~ can affect the removal of cloud and rainwater, ~~contributing to an increase in LWP (Bretherton et al., 2007). The impact of tunable parameters (Bretherton et al., 2007). While the MYNN3 PBL scheme parameterizes entrainment mixing reasonably well in the gray-zone (Ching et al., 2014), resolving sub-kilometer scales can result in weaker increases in liquid water path with aerosols due to fewer precipitating clouds and weaker LWP increase in non-raining clouds (Terai et al., 2020) within multi-scale climate models. Generally, these km-scale resolutions are well-suited~~  
515



520 [for resolving the cumulus outflow, but they may still be too coarse to resolve updrafts well \(Atlas et al., 2022\). The impacts of model caveats](#) like these on cloud cell expansion due to increased aerosol concentration ~~will~~ [should](#) be explored in subsequent research [with higher resolution models including large eddy simulations where the cloud-top entrainment interface can be modeled at finer spatial scale resolutions](#). It remains crucial to constrain such parameters based on observations (Suzuki and Stephens, 2009; Golaz et al., 2013; Christensen et al., 2023; Varble et al., 2023), where possible, to enhance our understanding  
525 of aerosol-cloud interactions and radiative forcing.

Overall, these ~~results~~ [WRF simulations](#) suggest that an increase in aerosol concentration may result in significantly more [radiative](#) cooling than would otherwise be predicted by the Twomey effect at the relatively short spatio-temporal-scales (300 km over 12 hours) considered here. We find generally that aerosols ~~elose~~ [expand the area of](#) stratocumulus cells, increase liquid water path, and cloud fraction. These relationships become enhanced in the presence of precipitation. Given the tight  
530 link between these radiative impacts and the nature of the mesoscale organization of clouds and its sensitivity to aerosol, it may be prudent to resolve these radiative effects in larger-scale models for improved assessments of climate change.

*Code and data availability.* All ARM and ACE-ENA products are available at <https://www.arm.gov/data/>. CERES SYN Ed4.1 product is available at <https://ceres.larc.nasa.gov>. MODIS collection 6 products are available at <https://earthdata.nasa.gov>. MERRA-2 data were obtained from <https://goldsmr4.gesdisc.eosdis.nasa.gov/data/MERRA-2/>. HYSPLIT trajectory code is available at <https://www.ready.noaa.gov/HYSPLIT.php>. An archive of the WRF namelist.input and trajectory files for each case study day are provided at [https://portal.nersc.gov/project/m1657/wrf\\_lagrangian\\_aci/](https://portal.nersc.gov/project/m1657/wrf_lagrangian_aci/) All data and code availability websites were last accessed on 10 October 2023.  
535

*Video supplement.* Movies S1 related to this article is available in the supplementary materials.

*Author contributions.* MWC wrote the manuscript and developed the Lagrangian trajectory approach and analysis. PW guided the implementation of the cloud segmentation algorithm. Research and development ideas, as well as writing and editing, were contributed by PW,  
540 ACV, HX, and JDF.

*Competing interests.* At least one of the (co-)authors is a member of the editorial board of Atmospheric Chemistry and Physics.

*Acknowledgements.* We would like to thank Yuwei Zhang for valuable feedback and assistance in compiling and running the WRF model. This research has been supported by the Atmospheric System Research (ASR) program as part of the US Department of Energy, Office of Science, Office of Biological and Environmental Research under Pacific Northwest National Laboratory (PNNL) project 57131. PNNL is

545 operated for the US Department of Energy by Battelle Memorial Institute under contract DE-A06-76RLO 1830. Observations from the ENA site and ACE-ENA campaign are supported by the Atmospheric Radiation Measurement (ARM) Climate Research Facility.

## References

- Abel, S. J., Boutle, I. A., Waite, K., Fox, S., Brown, P. R. A., Cotton, R., Lloyd, G., Choulaton, T. W., and Bower, K. N.: The Role of Precipitation in Controlling the Transition from Stratocumulus to Cumulus Clouds in a Northern Hemisphere Cold-Air Outbreak, *Journal of the Atmospheric Sciences*, 74, 2293 – 2314, <https://doi.org/https://doi.org/10.1175/JAS-D-16-0362.1>, 2017.
- 550 Ackerman, A. S., Kirkpatrick, M. P., Stevens, D. E., and Toon, O. B.: The Impact of Humidity above Stratiform Clouds on Indirect Aerosol Climate Forcing, *Nature*, 432, 1014–1017, <https://doi.org/10.1038/nature03174>, 2004.
- Albrecht, B. A.: Aerosols, Cloud Microphysics, and Fractional Cloudiness, *Science*, 245, 1227–1230, <https://doi.org/10.1126/science.245.4923.1227>, 1989.
- 555 Atlas, R. L., Bretherton, C. S., Khairoutdinov, M. F., and Blossey, P. N.: Hallett-Mossop Rime Splintering Dims Cumulus Clouds Over the Southern Ocean: New Insight From Nudged Global Storm-Resolving Simulations, *AGU Advances*, 3, e2021AV000454, <https://doi.org/https://doi.org/10.1029/2021AV000454>, e2021AV000454 2021AV000454, 2022.
- Barlage, M., Chen, F., Tewari, M., Ikeda, K., Gochis, D., Dudhia, J., Rasmussen, R., Livneh, B., Ek, M., and Mitchell, K.: Noah land surface model modifications to improve snowpack prediction in the Colorado Rocky Mountains, *Journal of Geophysical Research: Atmospheres*, 560 115, <https://doi.org/https://doi.org/10.1029/2009JD013470>, 2010.
- Bellouin, N., Quaas, J., Gryspeerdt, E., Kinne, S., Stier, P., Watson-Parris, D., Boucher, O., Carslaw, K. S., Christensen, M., Daniau, A.-L., Dufresne, J.-L., Feingold, G., Fiedler, S., Forster, P., Gettelman, A., Haywood, J. M., Lohmann, U., Malavelle, F., Mauritsen, T., McCoy, D. T., Myhre, G., Mülmenstädt, J., Neubauer, D., Possner, A., Rugenstein, M., Sato, Y., Schulz, M., Schwartz, S. E., Sourdeval, O., Storelvmo, T., Toll, V., Winker, D., and Stevens, B.: Bounding Global Aerosol Radiative Forcing of Climate Change, *Reviews of Geophysics*, 58, e2019RG000660, <https://doi.org/10.1029/2019RG000660>, 2020.
- 565 Bretherton, C. S., Blossey, P. N., and Uchida, J.: Cloud Droplet Sedimentation, Entrainment Efficiency, and Subtropical Stratocumulus Albedo, *Geophysical Research Letters*, 34, <https://doi.org/10.1029/2006gl027648>, 2007.
- Chen, Y.-C., Christensen, M. W., Stephens, G. L., and Seinfeld, J. H.: Satellite-Based Estimate of Global Aerosol-Cloud Radiative Forcing by Marine Warm Clouds, *Nature Geoscience*, 7, 643–646, <https://doi.org/10.1038/ngeo2214>, 2014.
- 570 Chin, M., Ginoux, P., Kinne, S., Torres, O., Holben, B. N., Duncan, B. N., Martin, R. V., Logan, J. A., Higurashi, A., and Nakajima, T.: Tropospheric aerosol optical thickness from the GOCART model and comparisons with satellite and Sun photometer measurements, *Journal of the Atmospheric Sciences*, 59, 461–483, [https://doi.org/Doi 10.1175/1520-0469\(2002\)059<0461:Taotft>2.0.Co;2](https://doi.org/Doi%2010.1175/1520-0469(2002)059%3C0461:Taotft%2E0.Co;2), 2002.
- Ching, J., Rotunno, R., LeMone, M., Martilli, A., Kosovic, B., Jimenez, P. A., and Dudhia, J.: Convectively Induced Secondary Circulations in Fine-Grid Mesoscale Numerical Weather Prediction Models, *Monthly Weather Review*, 142, 3284 – 3302, [https://doi.org/10.1175/MWR-](https://doi.org/10.1175/MWR-D-13-00318.1)
- 575 D-13-00318.1, 2014.
- Christensen, M. W. and Stephens, G. L.: Microphysical and Macrophysical Responses of Marine Stratocumulus Polluted by Underlying Ships: 2. Impacts of Haze on Precipitating Clouds, *Journal of Geophysical Research: Atmospheres*, 117, <https://doi.org/10.1029/2011JD017125>, 2012.
- Christensen, M. W., Suzuki, K., Zambri, B., and Stephens, G. L.: Ship Track Observations of a Reduced Shortwave Aerosol Indirect Effect in Mixed-Phase Clouds, *Geophysical Research Letters*, 41, 6970–6977, <https://doi.org/10.1002/2014GL061320>, 2014.
- 580 Christensen, M. W., Jones, W. K., and Stier, P.: Aerosols Enhance Cloud Lifetime and Brightness along the Stratus-to-Cumulus Transition, *Proc Natl Acad Sci U S A*, <https://doi.org/10.1073/pnas.1921231117>, 2020.

- Christensen, M. W., Ma, P.-L., Wu, P., Varble, A. C., Mülmenstädt, J., and Fast, J. D.: Evaluation of aerosol–cloud interactions in E3SM using a Lagrangian framework, *Atmospheric Chemistry and Physics*, 23, 2789–2812, <https://doi.org/10.5194/acp-23-2789-2023>, 2023.
- 585 Clothiaux, E. E., Miller, M. A., Perez, R. C., Turner, D. D., Moran, K. P., Martner, B. E., Ackerman, T. P., Mace, G. G., Marchand, R. T., Widener, K. B., Rodriguez, D. J., Uttal, T., Mather, J. H., Flynn, C. J., Gaustad, K. L., and Ermold, B.: The ARM Millimeter Wave Cloud Radars (MMCRs) and the Active Remote Sensing of Clouds (ARSCL) Value Added Product (VAP), NA, <https://doi.org/10.2172/1808567>, 2001.
- Diamond, M. S., Director, H. M., Eastman, R., Possner, A., and Wood, R.: Substantial Cloud Brightening From Shipping in Subtropical Low  
590 Clouds, *AGU Advances*, 1, e2019AV000 111, <https://doi.org/10.1029/2019AV000111>, 2020.
- Diamond, M. S., Saide, P. E., Zuidema, P., Ackerman, A. S., Doherty, S. J., Fridlind, A. M., Gordon, H., Howes, C., Kazil, J., Yamaguchi, T., Zhang, J., Feingold, G., and Wood, R.: Cloud adjustments from large-scale smoke–circulation interactions strongly modulate the southeastern Atlantic stratocumulus-to-cumulus transition, *Atmospheric Chemistry and Physics*, 22, 12 113–12 151, <https://doi.org/10.5194/acp-22-12113-2022>, 2022.
- 595 Eastman, R., Wood, R., and Bretherton, C. S.: Time Scales of Clouds and Cloud-Controlling Variables in Subtropical Stratocumulus from a Lagrangian Perspective, *Journal of the Atmospheric Sciences*, 73, 3079–3091, <https://doi.org/10.1175/JAS-D-16-0050.1>, 2016.
- Eastman, R., Terai, C. R., Grosvenor, D. P., and Wood, R.: Evaluating the Lagrangian Evolution of Subtropical Low Clouds in GCMs Using Observations: Mean Evolution, Time Scales, and Responses to Predictors, *Journal of the Atmospheric Sciences*, 78, 353 – 372, <https://doi.org/https://doi.org/10.1175/JAS-D-20-0178.1>, 2021.
- 600 Eirund, G. K., Lohmann, U., and Possner, A.: Cloud Ice Processes Enhance Spatial Scales of Organization in Arctic Stratocumulus, *Geophysical Research Letters*, 46, 14 109–14 117, <https://doi.org/https://doi.org/10.1029/2019GL084959>, 2019.
- Fan, M. and Pekour, M.: CPC\_ACEENA, <https://doi.org/10.5439/1440985>, 2018.
- Gelaro, R., McCarty, W., Suarez, M. J., Todling, R., Molod, A., Takacs, L., Randles, C. A., Darmenov, A., Bosilovich, M. G., Reichle, R., Wargan, K., Coy, L., Cullather, R., Draper, C., Akella, S., Buchard, V., Conaty, A., da Silva, A. M., Gu, W., Kim, G. K., Koster, R.,  
605 Lucchesi, R., Merkova, D., Nielsen, J. E., Partyka, G., Pawson, S., Putman, W., Rienecker, M., Schubert, S. D., Sienkiewicz, M., and Zhao, B.: The Modern-Era Retrospective Analysis for Research and Applications, Version 2 (MERRA-2), *Journal of Climate*, 30, 5419–5454, <https://doi.org/10.1175/Jcli-D-16-0758.1>, 2017.
- Ghate, V. P. and Cadetdu, M. P.: Drizzle and Turbulence Below Closed Cellular Marine Stratocumulus Clouds, *Journal of Geophysical Research-Atmospheres*, 124, 5724–5737, <https://doi.org/10.1029/2018jd030141>, 2019.
- 610 Golaz, J.-C., Horowitz, L. W., and Levy, H.: Cloud tuning in a coupled climate model: Impact on 20th century warming, *Geophysical Research Letters*, 40, 2246–2251, <https://doi.org/10.1002/grl.50232>, 2013.
- Goren, T. and Rosenfeld, D.: Decomposing aerosol cloud radiative effects into cloud cover, liquid water path and Twomey components in marine stratocumulus, *Atmospheric Research*, 138, 378 – 393, <https://doi.org/https://doi.org/10.1016/j.atmosres.2013.12.008>, 2014.
- Goren, T., Kazil, J., Hoffmann, F., Yamaguchi, T., and Feingold, G.: Anthropogenic Air Pollution Delays Marine Stratocumulus Break-up to  
615 Open-Cells, *Geophysical Research Letters*, 46, 14,135–14,144, <https://doi.org/10.1029/2019gl085412>, 2019.
- Grosvenor, D. P., Sourdeval, O., Zuidema, P., Ackerman, A., Alexandrov, M. D., Bennartz, R., Boers, R., Cairns, B., Chiu, J. C., Christensen, M., Deneke, H., Diamond, M., Feingold, G., Fridlind, A., Hunerbein, A., Knist, C., Kollias, P., Marshak, A., McCoy, D., Merk, D., Painemal, D., Rausch, J., Rosenfeld, D., Russchenberg, H., Seifert, P., Sinclair, K., Stier, P., van Diedenhoven, B., Wendisch, M., Werner, F., Wood, R., Zhang, Z., and Quaas, J.: Remote Sensing of Droplet Number Concentration in Warm Clouds: A Review of the Current  
620 State of Knowledge and Perspectives, *Reviews of Geophysics*, 56, 409–453, <https://doi.org/10.1029/2017RG000593>, 2018.

- Gryspeerd, E., Mülmenstädt, J., Gettelman, A., Malavelle, F. F., Morrison, H., Neubauer, D., Partridge, D. G., Stier, P., Takemura, T., Wang, H., Wang, M., and Zhang, K.: Surprising similarities in model and observational aerosol radiative forcing estimates, *Atmospheric Chemistry and Physics*, 20, 613–623, <https://doi.org/10.5194/acp-20-613-2020>, 2020.
- 625 Hallett, J. and Mossop, S.: Production of secondary ice particles during the riming process., *Nature*, 249, 26–28, <https://doi.org/https://doi.org/10.1038/249026a0>, 1974.
- Hardin, J., Giangrande, S. E., and Zhou, A.: Laser Disdrometer Quantities (LDQUANTS) and Video Disdrometer Quantities (VDIS-QUANTS) Value-Added Products Report, <https://doi.org/10.2172/1808573>, 2020.
- Hong, S. Y., Noh, Y., and Dudhia, J.: A new vertical diffusion package with an explicit treatment of entrainment processes, *Monthly Weather Review*, 134, 2318–2341, <https://doi.org/Doi.10.1175/Mwr3199.1>, 2006.
- 630 Hu, X.-M., Nielsen-Gammon, J. W., and Zhang, F.: Evaluation of Three Planetary Boundary Layer Schemes in the WRF Model, *Journal of Applied Meteorology and Climatology*, 49, 1831 – 1844, <https://doi.org/https://doi.org/10.1175/2010JAMC2432.1>, 2010.
- Iacono, M. J., Delamere, J. S., Mlawer, E. J., Shephard, M. W., Clough, S. A., and Collins, W. D.: Radiative forcing by long-lived greenhouse gases: Calculations with the AER radiative transfer models, *Journal of Geophysical Research: Atmospheres*, 113, <https://doi.org/https://doi.org/10.1029/2008JD009944>, 2008.
- 635 Jensen, M. P., Ghate, V. P., Wang, D., Apoznanski, D. K., Bartholomew, M. J., Giangrande, S. E., Johnson, K. L., and Thieman, M. M.: Contrasting characteristics of open- and closed-cellular stratocumulus cloud in the eastern North Atlantic, *Atmospheric Chemistry and Physics*, 21, 14 557–14 571, <https://doi.org/10.5194/acp-21-14557-2021>, 2021.
- Jimenez, P. A., Hacker, J. P., Dudhia, J., Haupt, S. E., Ruiz-Arias, J. A., Gueymard, C. A., Thompson, G., Eidhammer, T., and Deng, A.: WRF-Solar: Description and Clear-Sky Assessment of an Augmented NWP Model for Solar Power Prediction, *Bulletin of the American Meteorological Society*, 97, 1249 – 1264, <https://doi.org/10.1175/BAMS-D-14-00279.1>, 2016.
- 640 Kazil, J., Christensen, M. W., Abel, S. J., Yamaguchi, T., and Feingold, G.: Realism of Lagrangian Large Eddy Simulations Driven by Reanalysis Meteorology: Tracking a Pocket of Open Cells Under a Biomass Burning Aerosol Layer, *Journal of Advances in Modeling Earth Systems*, 13, e2021MS002 664, <https://doi.org/https://doi.org/10.1029/2021MS002664>, e2021MS002664 2021MS002664, 2021.
- Kollias, P., Clothiaux, E. E., Ackerman, T. P., Albrecht, B. A., Widener, K. B., Moran, K. P., Luke, E. P., Johnson, K. L., Bharadwaj, N., 645 Mead, J. B., Miller, M. A., Verlinde, J., Marchand, R. T., and Mace, G. G.: Development and Applications of ARM Millimeter-Wavelength Cloud Radars, *Meteorological Monographs*, 57, 17.1 – 17.19, <https://doi.org/10.1175/AMSMONOGRAPHS-D-15-0037.1>, 2016.
- Lewis, H., Bellon, G., and Dinh, T.: Upstream Large-Scale Control of Subtropical Low-Cloud Climatology, *Journal of Climate*, 36, 3289 – 3303, <https://doi.org/https://doi.org/10.1175/JCLI-D-22-0676.1>, 2023.
- Lohmann, U.: A glaciation indirect aerosol effect caused by soot aerosols, *Geophysical Research Letters*, 29, 11–1–11–4, 650 <https://doi.org/https://doi.org/10.1029/2001GL014357>, 2002.
- Malavelle, F. F., Haywood, J. M., Jones, A., Gettelman, A., Clarisse, L., Bauduin, S., Allan, R. P., Karset, I. H. H., Kristjánsson, J. E., Oreopoulos, L., Cho, N., Lee, D., Bellouin, N., Boucher, O., Grosvenor, D. P., Carslaw, K. S., Dhomse, S., Mann, G. W., Schmidt, A., Coe, H., Hartley, M. E., Dalvi, M., Hill, A. A., Johnson, B. T., Johnson, C. E., Knight, J. R., O’Connor, F. M., Partridge, D. G., Stier, P., Myhre, G., Platnick, S., Stephens, G. L., Takahashi, H., and Thordarson, T.: Strong Constraints on Aerosol–Cloud Interactions from 655 Volcanic Eruptions, *Nature*, 546, 485–491, <https://doi.org/10.1038/nature22974>, 2017.
- Matthews, A. and Mei, F.: WCM water content for ACE-ENA, <https://doi.org/10.5439/1465759>, united States, 2017.
- Mellor, G. L. and Yamada, T.: Development of a Turbulence Closure-Model for Geophysical Fluid Problems, *Reviews of Geophysics*, 20, 851–875, <https://doi.org/DOI.10.1029/RG020i004p00851>, 1982.

- 660 Miller, M. A., Mages, Z., Zheng, Q., Trabachino, L., Russell, L. M., Shilling, J. E., and Zawadowicz, M. A.: Observed Relationships Between Cloud Droplet Effective Radius and Biogenic Gas Concentrations in Summertime Marine Stratocumulus Over the Eastern North Atlantic, *Earth and Space Science*, 9, e2021EA001929, <https://doi.org/https://doi.org/10.1029/2021EA001929>, e2021EA001929 2021EA001929, 2022.
- Min, Q. and Harrison, L. C.: Cloud properties derived from surface MFRSR measurements and comparison with GOES results at the ARM SGP Site, *Geophysical Research Letters*, 23, 1641–1644, <https://doi.org/https://doi.org/10.1029/96GL01488>, 1996.
- 665 Morrison, H., Curry, J. A., and Khvorostyanov, V. I.: A New Double-Moment Microphysics Parameterization for Application in Cloud and Climate Models. Part I: Description, *Journal of the Atmospheric Sciences*, 62, 1665 – 1677, <https://doi.org/https://doi.org/10.1175/JAS3446.1>, 2005.
- Mülmenstädt, J., Nam, C., Salzmann, M., Kretzschmar, J., L'Ecuyer, T. S., Lohmann, U., Ma, P.-L., Myhre, G., Neubauer, D., Stier, P., Suzuki, K., Wang, M., and Quaas, J.: Reducing the aerosol forcing uncertainty using observational constraints on warm rain processes, *Science Advances*, 6, eaaz6433, <https://doi.org/10.1126/sciadv.aaz6433>, 2020.
- 670 Nakanishi, M. and Niino, H.: Development of an Improved Turbulence Closure Model for the Atmospheric Boundary Layer, *Journal of the Meteorological Society of Japan*, 87, 895–912, <https://doi.org/10.2151/jmsj.87.895>, 2009.
- O'Connor, E. J., Illingworth, A. J., and Hogan, R. J.: A Technique for Autocalibration of Cloud Lidar, *Journal of Atmospheric and Oceanic Technology*, 21, 777 – 786, [https://doi.org/10.1175/1520-0426\(2004\)021<0777:ATFAOC>2.0.CO;2](https://doi.org/10.1175/1520-0426(2004)021<0777:ATFAOC>2.0.CO;2), 2004.
- 675 Otkin, J. A. and Greenwald, T. J.: Comparison of WRF Model-Simulated and MODIS-Derived Cloud Data, *Monthly Weather Review*, 136, 1957 – 1970, <https://doi.org/10.1175/2007MWR2293.1>, 2008.
- Pincus, R. and Baker, M. B.: Effect of precipitation on the albedo susceptibility of clouds in the marine boundary layer, *Nature*, 372, 250–252, 1994.
- Pincus, R., Barker, H. W., and Morcrette, J.-J.: A fast, flexible, approximate technique for computing radiative transfer in inhomogeneous cloud fields, *Journal of Geophysical Research: Atmospheres*, 108, <https://doi.org/https://doi.org/10.1029/2002JD003322>, 2003.
- 680 Pinker, R. T., Ma, Y. T., Chen, W., Laszlo, I., Liu, H. Q., Kim, H. Y., and Daniels, J.: Top-of-the-atmosphere reflected shortwave radiative fluxes from GOES-R, *Atmospheric Measurement Techniques*, 15, 5077–5094, <https://doi.org/10.5194/amt-15-5077-2022>, 2022.
- Platnick, S.: Vertical photon transport in cloud remote sensing problems, *Journal of Geophysical Research: Atmospheres*, 105, 22 919–22 935, 2000.
- 685 Platnick, S., Meyer, K. G., King, M. D., Wind, G., Amarasinghe, N., Marchant, B., Arnold, G. T., Zhang, Z., Hubanks, P. A., Holz, R. E., Yang, P., Ridgway, W. L., and Riedi, J.: The MODIS Cloud Optical and Microphysical Products: Collection 6 Updates and Examples From Terra and Aqua, *IEEE Transact. Geosci. Remote Sens.*, 55, 502–525, <https://doi.org/10.1109/TGRS.2016.2610522>, 2017.
- Quaas, J., Boucher, O., Bellouin, N., and Kinne, S.: Satellite-based estimate of the direct and indirect aerosol climate forcing, *Journal of Geophysical Research: Atmospheres*, 113, <https://doi.org/10.1029/2007JD008962>, 2008.
- 690 Randall, D. A., J. A. Coakley Jr., Fairall, C. W., Kropfli, R. A., and Lenschow, D. H.: Outlook for research on subtropical marine stratiform clouds, *Bull. Amer. Meteor. Soc.*, 65, 1290–1301, 1984.
- Rosenfeld, D., Kaufman, Y. J., and Koren, I.: Switching cloud cover and dynamical regimes from open to closed Benard cells in response to the suppression of precipitation by aerosols, *Atmospheric Chemistry and Physics*, 6, 2503–2511, <https://doi.org/10.5194/acp-6-2503-2006>, 2006.

- 695 Rutan, D. A., Kato, S., Doelling, D. R., Rose, F. G., Nguyen, L. T., Caldwell, T. E., and Loeb, N. G.: CERES Synoptic Product: Methodology and Validation of Surface Radiant Flux, *Journal of Atmospheric and Oceanic Technology*, 32, 1121–1143, <https://doi.org/10.1175/JTECH-D-14-00165.1>, 2015.
- Seifert, A., Heus, T., Pincus, R., and Stevens, B.: Large-Eddy Simulation of the Transient and near-Equilibrium Behavior of Precipitating Shallow Convection, *Journal of Advances in Modeling Earth Systems*, 7, 1918–1937, <https://doi.org/10.1002/2015ms000489>, 2015.
- 700 Seinfeld, J. H., Bretherton, C., Carslaw, K. S., Coe, H., DeMott, P. J., Dunlea, E. J., Feingold, G., Ghan, S., Guenther, A. B., Kahn, R., Kraucunas, I., Kreidenweis, S. M., Molina, M. J., Nenes, A., Penner, J. E., Prather, K. A., Ramanathan, V., Ramaswamy, V., Rasch, P. J., Ravishankara, A. R., Rosenfeld, D., Stephens, G., and Wood, R.: Improving our fundamental understanding of the role of aerosol-cloud interactions in the climate system, *Proceedings of the National Academy of Sciences*, 113, 5781–5790, <https://doi.org/10.1073/pnas.1514043113>, 2016.
- 705 Skamarock, W. C., Klemp, J. B., Dudhia, J., Gill, D. O., Liu, Z., Berner, J., Wang, W., Powers, J. G., Duda, M. G., Barker, D., and Huang, X.: A Description of the Advanced Research WRF Model Version 4.3 (No. NCAR/TN-556+STR), <https://doi.org/doi:10.5065/1dfh-6p97>, 2021.
- Small, J. D., Chuang, P. Y., Feingold, G., and Jiang, H.: Can aerosol decrease cloud lifetime?, *Geophysical Research Letters*, 36, <https://doi.org/10.1029/2009GL038888>, 2009.
- 710 Stein, A. F., Draxler, R. R., Rolph, G. D., Stunder, B. J. B., Cohen, M. D., and Ngan, F.: NOAA’s HYSPLIT Atmospheric Transport and Dispersion Modeling System, *Bulletin of the American Meteorological Society*, 96, 2059 – 2077, <https://doi.org/https://doi.org/10.1175/BAMS-D-14-00110.1>, 2015.
- Stephens, G. L.: Radiation profiles in extended water clouds. II: Parameterization schemes, *Journal of the Atmospheric Sciences*, 35, 2123–2132, 1978.
- 715 Suzuki, K. and Stephens, G. L.: Relationship between radar reflectivity and the time scale of warm rain formation in a global cloud-resolving model, *Atmos. Res.*, 12.010, doi:10.1016/j.atmosres., 2009.
- Tang, S. and Xie, S.: Atmospheric Radiation Measurement (ARM) user facility, 2020: ARM Best Estimate Cloud Radiation (ARMBE-CLDRAD). 2014-01-01 to 2020-12-31, Eastern North Atlantic (ENA) Graciosa Island, Azores, Portugal (C1), doi:10.5439/1333228., data set accessed 2022-01-19 at doi:10.5439/1333228., 2020.
- 720 Terai, C. R., Pritchard, M. S., Blossey, P., and Bretherton, C. S.: The Impact of Resolving Subkilometer Processes on Aerosol-Cloud Interactions of Low-Level Clouds in Global Model Simulations, *Journal of Advances in Modeling Earth Systems*, 12, e2020MS002274, <https://doi.org/https://doi.org/10.1029/2020MS002274>, e2020MS002274 10.1029/2020MS002274, 2020.
- Thompson, G. and Eidhammer, T.: A Study of Aerosol Impacts on Clouds and Precipitation Development in a Large Winter Cyclone, *Journal of the Atmospheric Sciences*, 71, 3636 – 3658, <https://doi.org/10.1175/JAS-D-13-0305.1>, 2014.
- 725 Thompson, G., Tewari, M., Ikeda, K., Tessendorf, S., Weeks, C., Otkin, J., and Kong, F.: Explicitly-coupled cloud physics and radiation parameterizations and subsequent evaluation in WRF high-resolution convective forecasts, *Atmospheric Research*, 168, 92–104, <https://doi.org/https://doi.org/10.1016/j.atmosres.2015.09.005>, 2016.
- Tokay, A., Wolff, D. B., and Petersen, W. A.: Evaluation of the New Version of the Laser-Optical Disdrometer, OTT Parsivel2, *Journal of Atmospheric and Oceanic Technology*, 31, 1276 – 1288, <https://doi.org/10.1175/JTECH-D-13-00174.1>, 2014.
- 730 Toll, V., Christensen, M., Gasso, S., and Bellouin, N.: Volcano and Ship Tracks Indicate Excessive Aerosol-Induced Cloud Water Increases in a Climate Model, *Geophysical Research Letters*, 44, 12,492–12,500, <https://doi.org/10.1002/2017GL075280>, 2017.
- Troyan, D.: Interpolated Sounding Value-Added Product, <https://doi.org/10.2172/1226794>, 2013.

- Turner, D., Q. C. L., Zhang, M. D., and Gaustad, K.: Atmospheric Radiation Measurement (ARM) user facility, 2021: Cloud Optical Properties from the Multifilter Shadowband Radiometer (MFRSRCLDOD): An ARM Value-Added Product. 2014-06-01 to 2019-10-27, Eastern North Atlantic (ENA) Graciosa Island, Azores, Portugal (C1)., <https://www.arm.gov/capabilities/vaps/mfrsrclod>, data set accessed 2022-01-19 at <https://www.arm.gov/capabilities/vaps/mfrsrclod>, 2021.
- 735 Uin, J. and Mei, F.: Cloud Condensation Nuclei Particle Counter Instrument Handbook - Airborne Version, <https://doi.org/10.2172/1562677>, 2019.
- Varble, A. C., Ma, P.-L., Christensen, M. W., Mülmenstädt, J., Tang, S., and Fast, J.: Evaluation of Liquid Cloud Albedo Susceptibility in E3SM Using Coupled Eastern North Atlantic Surface and Satellite Retrievals, *EGUsphere*, 2023, 1–39, <https://doi.org/10.5194/egusphere-2023-998>, 2023.
- 740 Wang, H. and Feingold, G.: Modeling mesoscale cellular structures and drizzle in marine stratocumulus. Part II: The microphysics and dynamics of the boundary region between open and closed cells, *Journal of the Atmospheric Sciences*, 66, 3257–3275, doi:10.1175/2009JAS3120.1, 2009.
- 745 Wang, J., Wood, R., Jensen, M. P., Chiu, J. C., Liu, Y., Lamer, K., Desai, N., Giangrande, S. E., Knopf, D. A., Kollias, P., Laskin, A., Liu, X., Lu, C., Mechem, D., Mei, F., Starzec, M., Tomlinson, J., Wang, Y., Yum, S. S., Zheng, G., Aiken, A. C., Azevedo, E. B., Blanchard, Y., China, S., Dong, X., Gallo, F., Gao, S., Ghate, V. P., Glienke, S., Goldberger, L., Hardin, J. C., Kuang, C., Luke, E. P., Matthews, A. A., Miller, M. A., Moffet, R., Pekour, M., Schmid, B., Sedlacek, A. J., Shaw, R. A., Shilling, J. E., Sullivan, A., Suski, K., Veghte, D. P., Weber, R., Wyant, M., Yeom, J., Zawadowicz, M., and Zhang, Z.: Aerosol and Cloud Experiments in the Eastern North Atlantic (ACE-ENA), *Bulletin of the American Meteorological Society*, 103, E619 – E641, <https://doi.org/https://doi.org/10.1175/BAMS-D-19-0220.1>, 2022.
- 750 Wang, Y., Zheng, X. J., Dong, X. Q., Xi, B. K., Wu, P., Logan, T., and Yung, Y. L.: Impacts of long-range transport of aerosols on marine-boundary-layer clouds in the eastern North Atlantic, *Atmospheric Chemistry and Physics*, 20, 14 741–14 755, <https://doi.org/10.5194/acp-20-14741-2020>, 2020.
- Wood, R.: Drizzle in Stratiform Boundary Layer Clouds. Part I: Vertical and Horizontal Structure, *Journal of the Atmospheric Sciences*, 62, 3011–3033, doi:10.1175/JAS3529.1, 2005.
- 755 Wood, R.: Stratocumulus Clouds, *Mon. Wea. Rev.*, 140, 2373?2423, 2012.
- Wood, R. and Hartmann, D. L.: Spatial variability of liquid water path in marine low cloud: the importance of mesoscale cellular convection, *Journal of Climate*, 19, 1748–1764, doi: 10.1175/JCLI3702.1, 2006.
- Wu, P. and Ovchinnikov, M.: Cloud Morphology Evolution in Arctic Cold-Air Outbreak: Two Cases During COMBLE Period, *Journal of Geophysical Research: Atmospheres*, 127, e2021JD035 966, <https://doi.org/https://doi.org/10.1029/2021JD035966>, e2021JD035966 2021JD035966, 2022.
- 760 Xie, S., McCoy, R. B., Klein, S. A., Cederwall, R. T., Wiscombe, W. J., Jensen, M. P., Johnson, K. L., Clothiaux, E. E., Gaustad, K. L., Long, C. N., Mather, J. H., McFarlane, S. A., Shi, Y., Golaz, J.-C., Lin, Y., Hall, S. D., McCord, R. A., Palanisamy, G., and Turner, D. D.: CLOUDS AND MORE: ARM Climate Modeling Best Estimate Data: A New Data Product for Climate Studies, *Bulletin of the American Meteorological Society*, 91, 13 – 20, <https://doi.org/10.1175/2009BAMS2891.1>, 2010.
- 765 Yamaguchi, T., Feingold, G., and Kazil, J.: Stratocumulus to Cumulus Transition by Drizzle, *Journal of Advances in Modeling Earth Systems*, 9, 2333–2349, <https://doi.org/10.1002/2017MS001104>, 2017.
- Zhang, C. X., Wang, Y. Q., and Hamilton, K.: Improved Representation of Boundary Layer Clouds over the Southeast Pacific in ARW-WRF Using a Modified Tiedtke Cumulus Parameterization Scheme, *Monthly Weather Review*, 139, 3489–3513, <https://doi.org/10.1175/Mwr-D-10-05091.1>, 2011.
- 770



- Zhang, X., Huang, X.-Y., Liu, J., Poterjoy, J., Weng, Y., Zhang, F., and Wang, H.: Development of an Efficient Regional Four-Dimensional Variational Data Assimilation System for WRF, *Journal of Atmospheric and Oceanic Technology*, 31, 2777 – 2794, <https://doi.org/10.1175/JTECH-D-13-00076.1>, 2014.
- 775 Zheng, X. J., Dong, X. Q., Ward, D. M., Xi, B. K., Wu, P., and Wang, Y.: Aerosol-Cloud-Precipitation Interactions in a Closed-cell and Non-homogenous MBL Stratocumulus Cloud, *Advances in Atmospheric Sciences*, 39, 2107–2123, <https://doi.org/10.1007/s00376-022-2013-6>, 2022a.
- Zheng, X. J., Xi, B. K., Dong, X. Q., Wu, P., Logan, T., and Wang, Y.: Environmental effects on aerosol-cloud interaction in non-precipitating marine boundary layer (MBL) clouds over the eastern North Atlantic, *Atmospheric Chemistry and Physics*, 22, 335–354, <https://doi.org/10.5194/acp-22-335-2022>, 2022b.
- 780 Zheng, Y., Rosenfeld, D., and Li, Z.: Estimating the Decoupling Degree of Subtropical Marine Stratocumulus Decks From Satellite, *Geophysical Research Letters*, 45, 12,560–12,568, <https://doi.org/https://doi.org/10.1029/2018GL078382>, 2018.
- Zhou, X., Ackerman, A. S., Fridlind, A. M., and Kollias, P.: Simulation of Mesoscale Cellular Convection in Marine Stratocumulus. Part I: Drizzling Conditions, *Journal of the Atmospheric Sciences*, 75, 257 – 274, <https://doi.org/https://doi.org/10.1175/JAS-D-17-0070.1>, 2018.

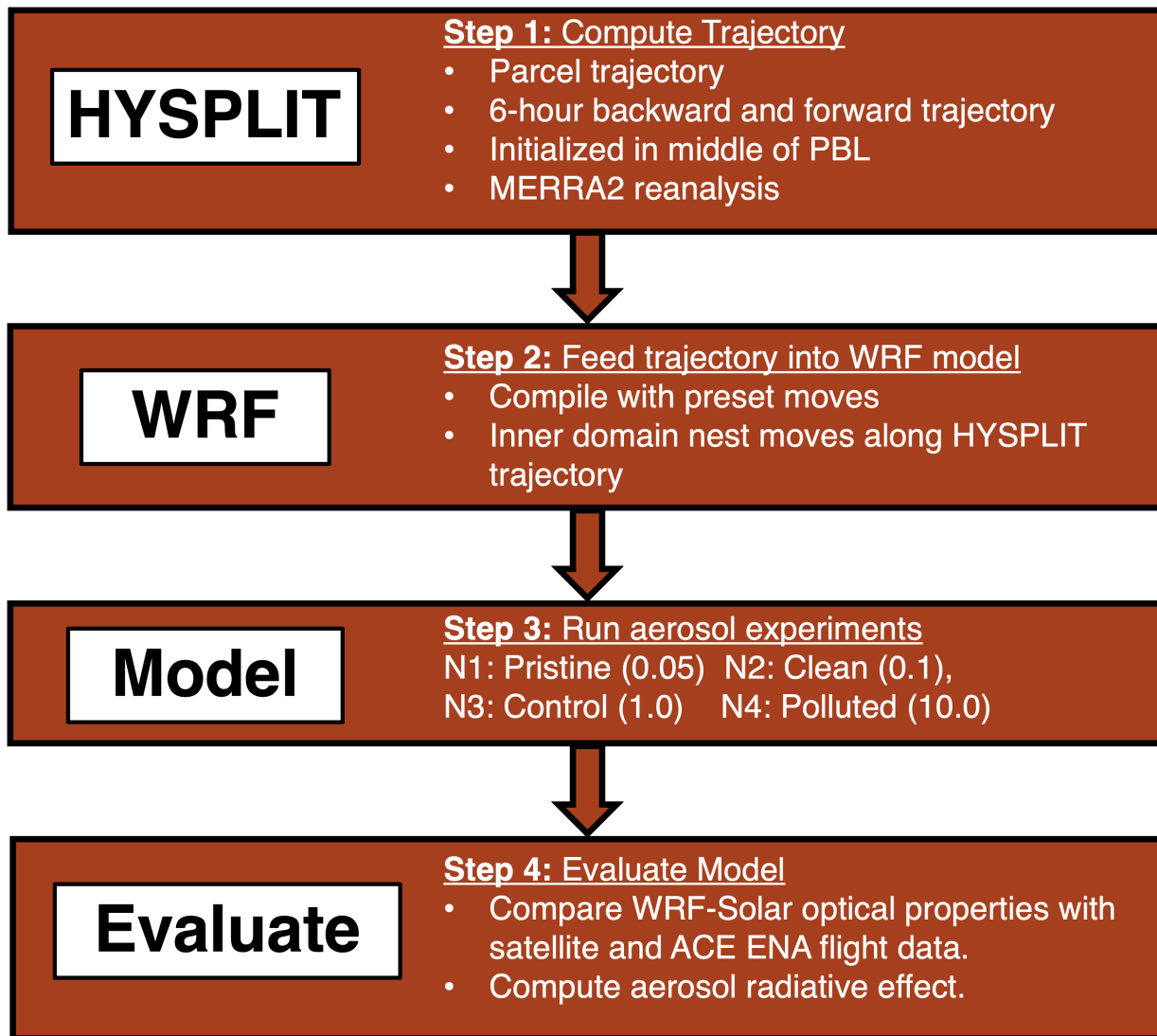


**Figure 1.** Flow chart showing depicting the methodology of implementing the Lagrangian framework for studying aerosol-cloud interactions in a Lagrangian framework using the WRF model.

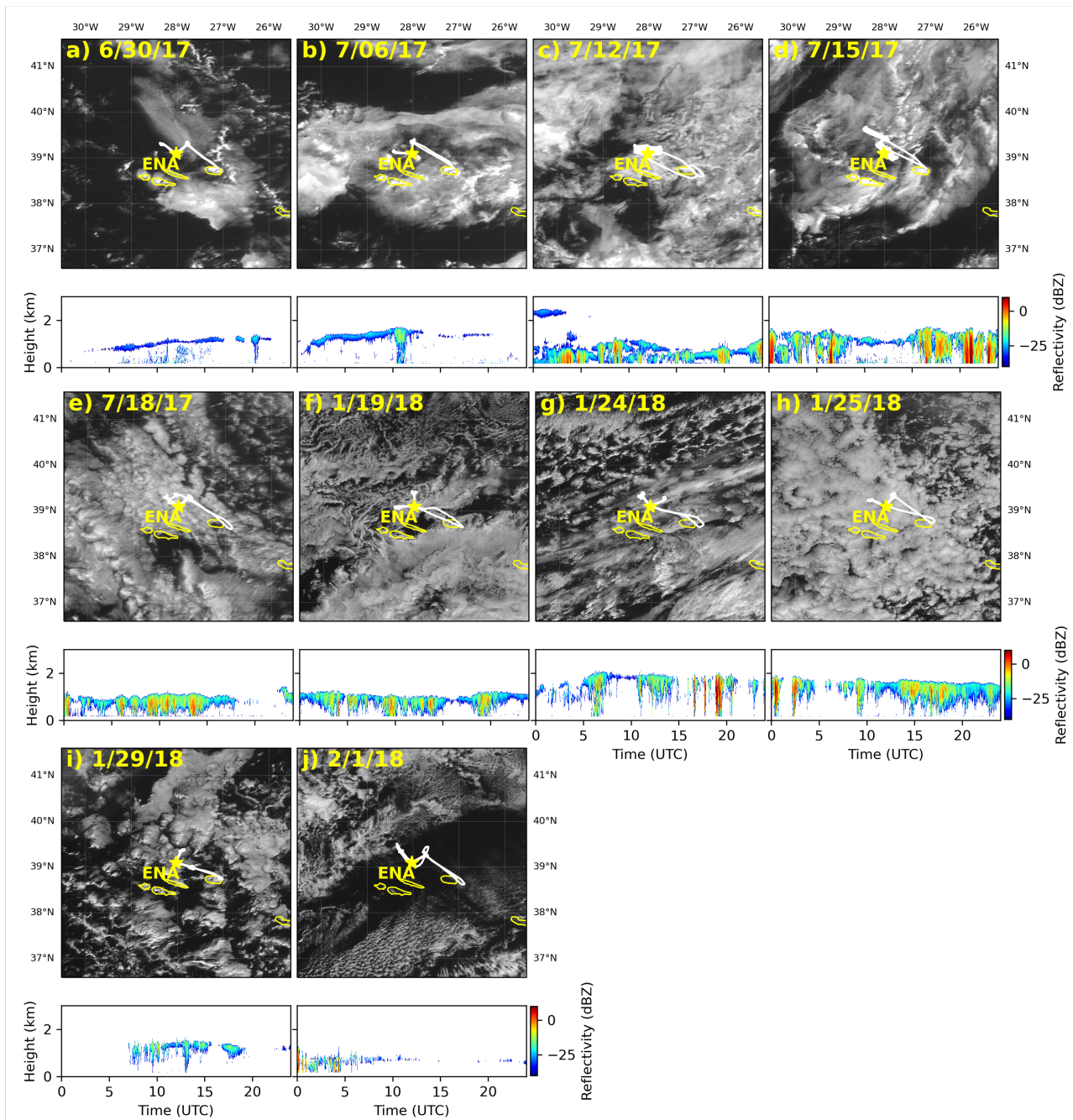


**Figure 2.** Case studies during summer (a - e) and winter (f - j) ACE-ENA IOP periods. Panels [display show](#) GOES visible images at 13:00 UTC displayed over  $4 \times 4^\circ$  regions centered over Graciosa Island (yellow star denotes the ARM site). Aircraft flight positions are shown as white lines. Vertically pointing Ka-band reflectivity at the ARM site is displayed over a 24-hr period for the corresponding days.

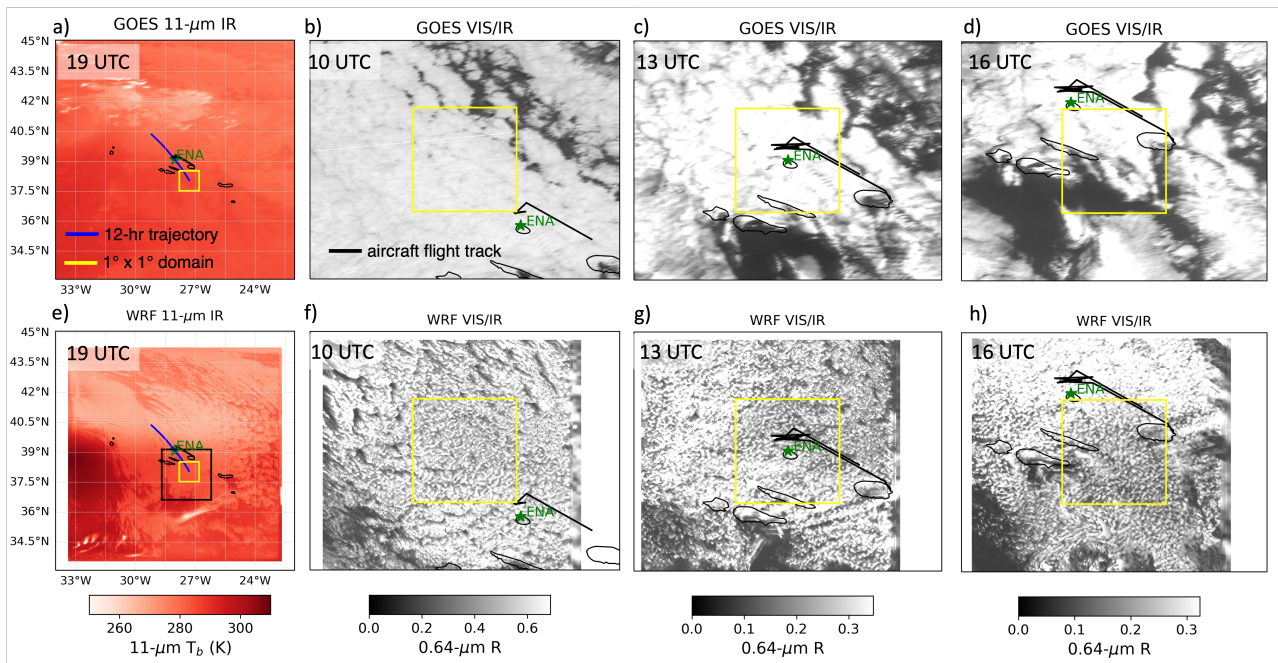


**Figure 3.** GOES  $11\text{-}\mu\text{m}$   $11\text{-}\mu\text{m}$  thermal infrared image at on 07/18/2017 at 19:00 UTC is centered over the Graciosa island with the positions of along the HYSPLIT trajectory computed using ERA5 reanalysis is plotted in (blue line) a). The yellow box denotes a  $1 \times 1^\circ$  region that moves along the center of the trajectory. Visible imagery at  $0.64\text{-}\mu\text{m}$  reflectance over a larger  $2 \times 2^\circ$  region is shown at discrete times (10, 13, and 16 UTC; b, c, d respectively). Similarly, the WRF simulations of the brightness temperature at  $11\text{-}\mu\text{m}$  and normalized shortwave albedo is are displayed at the same times (e, f, g, and h). The black line denotes aircraft observations from the ACE-ENA campaign.

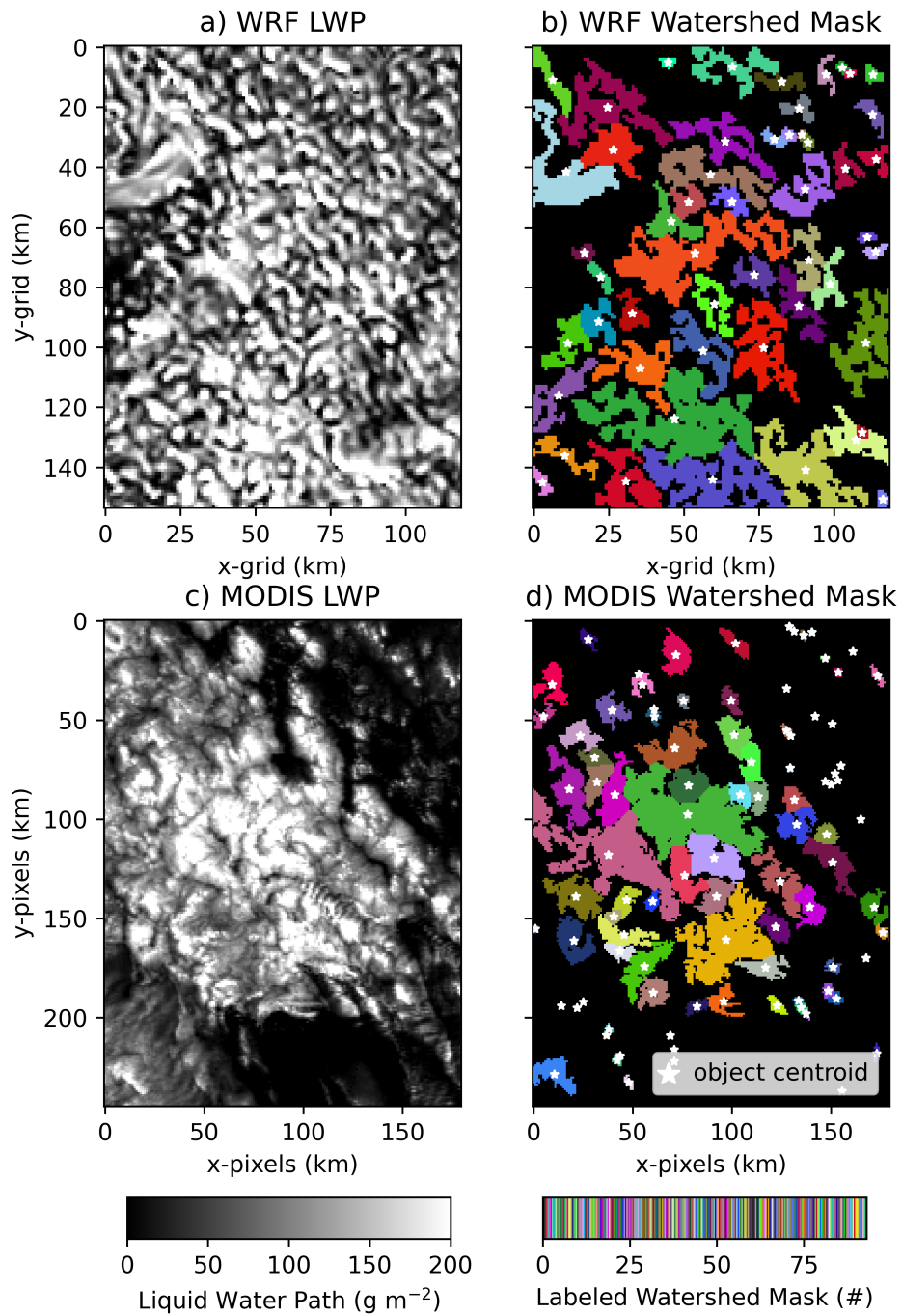


**Figure 4.** Liquid water path and watershed regions for WRF (a and b) and MODIS (c and d) ~~in the case study occurring~~ on 07/18/2017 at 13 UTC. White stars indicate object centroid locations.

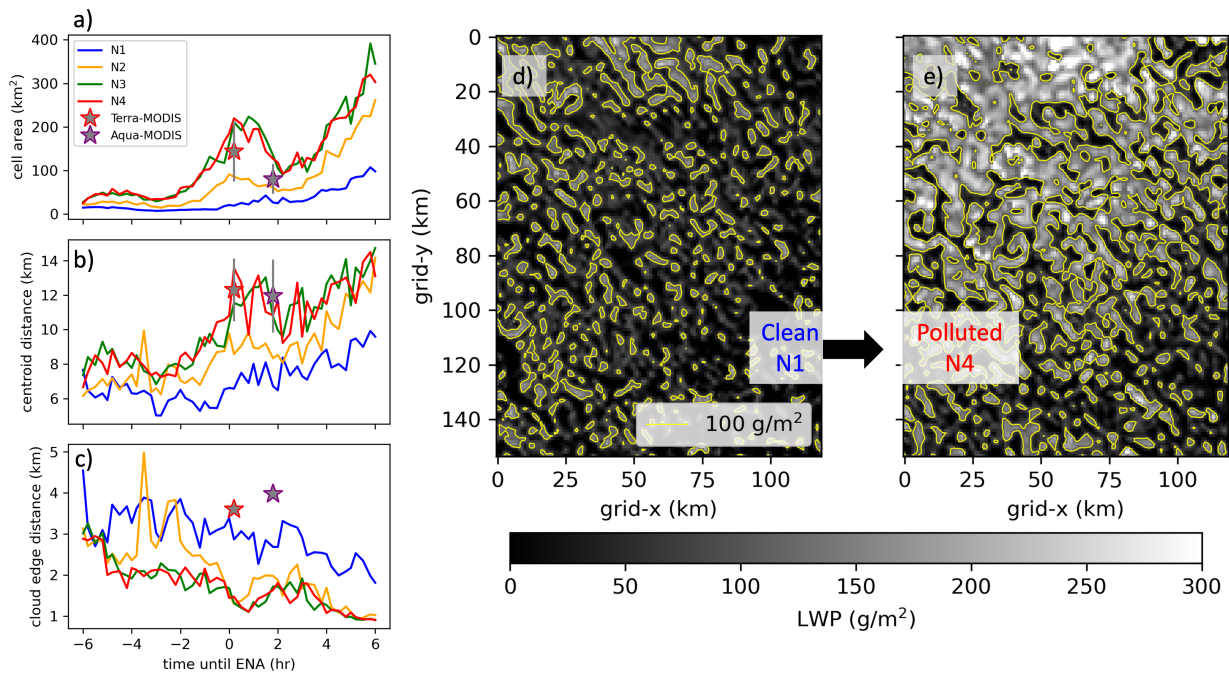


**Figure 5.** Time-series of the average (a) cloud object area, (b) minimum distance between cloud centroids, (c) minimum distance between cloud edges over each 15-minute time-interval detected for ultra-clean-pristine (blue), clean (orange), control (green), and polluted (red) experiments in the case study occurring on 07/18/2017. MODIS averages (star) and standard deviations (vertical lines) are displayed on the image. Images of the LWP at 13 UTC is displayed for the clean (d) and polluted experiments (e).

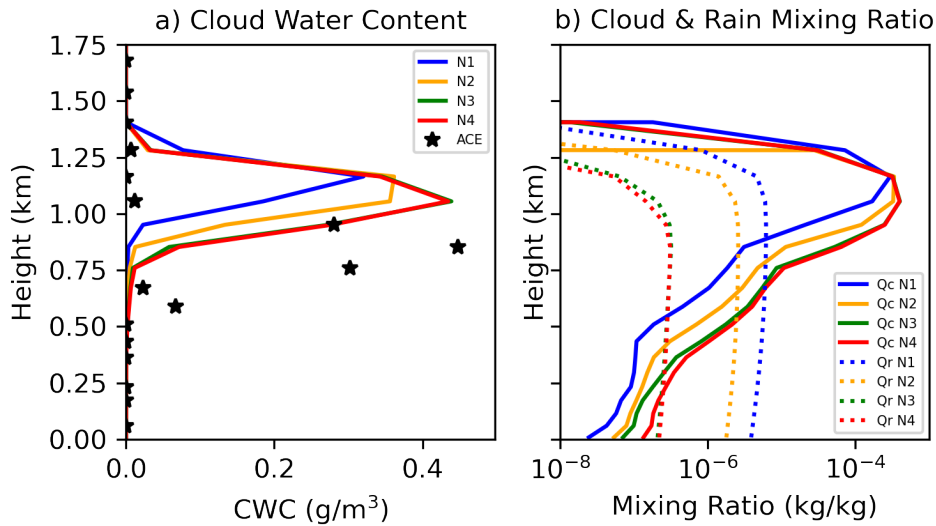


**Figure 6.** a) Vertical profile of the cloud-total water content measured by the G-1 aircraft in the WCM-2000 data product during the ACE-ENA flight (stars) on 07/18/2017 is averaged over an hour across the domain from 13-14 UTC (path-of-the-The flight path is shown-illustrated in Figure 3 and simulated for pristine (N1; blue), clean (N2; orange), control (N3; green), and polluted (N4; red) experiments. b) Vertical Additionally, the simulated vertical profile of cloud (solid) and rain (dotted) water mixing ratios is averaged over the domain for each aerosol experiment.

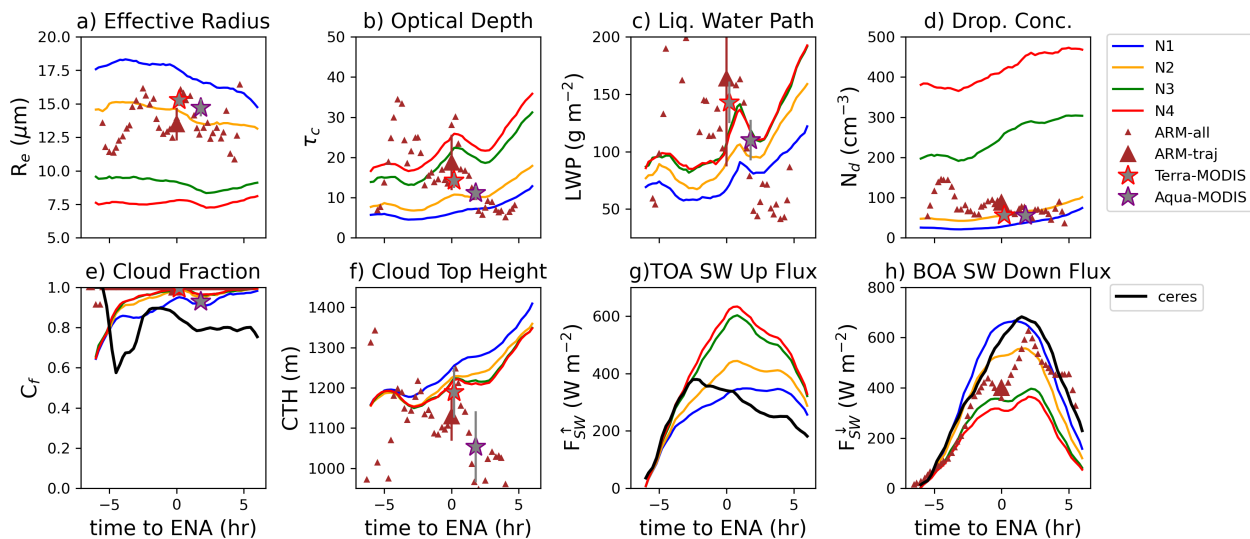


**Figure 7.** a) Droplet effective radius ( $R_e$ ), b) cloud optical thickness ( $\tau_c$  retrieved from the 3.7- $\mu\text{m}$  band), c) liquid water path (LWP), d) droplet concentration ( $N_d$ ) computed from  $R_e$  and  $\tau_c$ , e) liquid cloud fraction ( $C_f$ ), f) cloud top height (CTH), g) top of atmosphere outgoing shortwave radiative flux ( $F_{SW}^{\uparrow}$ , and h) bottom of atmosphere incoming shortwave flux ( $F_{SW}^{\downarrow}$  for pristine (blue), clean (orange), control (green), and polluted (red) WRF simulations. WRF-Solar was used for comparison with the satellite retrievals. ARM (brown diamond) retrievals are provided at all time steps and at the time when the trajectory passes over the ARM site (larger brown diamond) and MODIS retrievals from satellites Terra (red star) and Aqua (blue star) are provided when available along the trajectory on 07/18/2017. [Hourly retrievals of the cloud fraction and radiative fluxes are provided by CERES.](#) Note, aside from time to ENA equals 0, the ARM measurements do not coincide with the trajectory location and are merely used to show Eulerian variability.



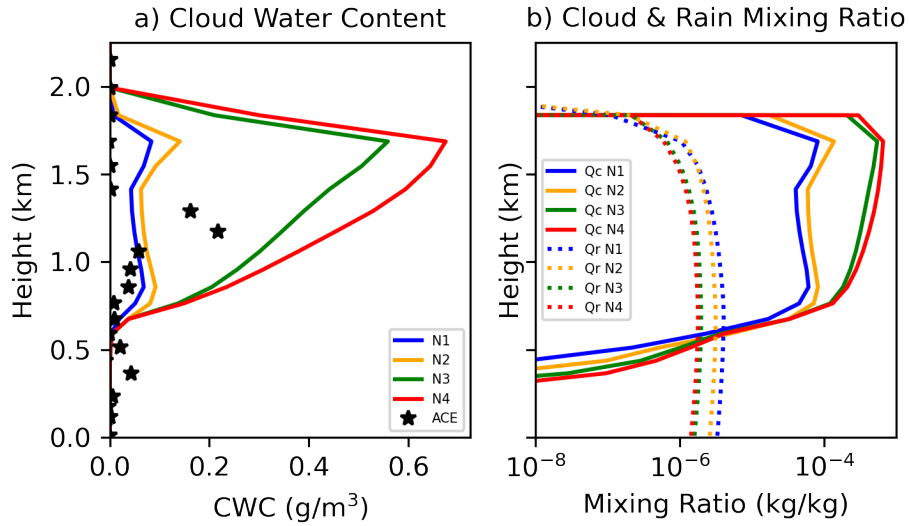


**Figure 8.** a) Vertical profile of the cloud water content measured during the ACE-ENA flight (stars) on [Same as Figure 6 except for case study 07/15/2017 averaged over an hour across the domain from 13-14 UTC](#) (path of the flight is shown in Figure 3 and simulated for pristine (N1; blue), clean (N2; orange), control (N3; green), and polluted (N4; red) experiments. b) Vertical profile of cloud (solid) and rain (dotted) water mixing ratios averaged over the domain for each aerosol experiment. [2017.](#)

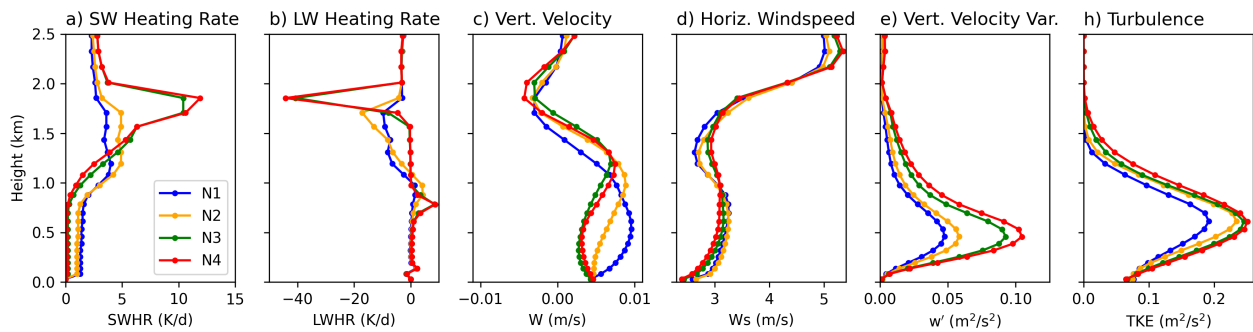


**Figure 9.** Vertical profile of the a) mean shortwave and b) longwave radiative heating rate, c) mean vertical velocity, d) mean horizontal wind speed, e) vertical velocity variance, and h) ~~2-times the~~ turbulent kinetic energy (TKE; ~~QKE is twice the~~ TKE) for pristine (blue), unpolluted (orange), control (green), and polluted (red) WRF simulations on 07/15/2017 at 13:00 UTC.

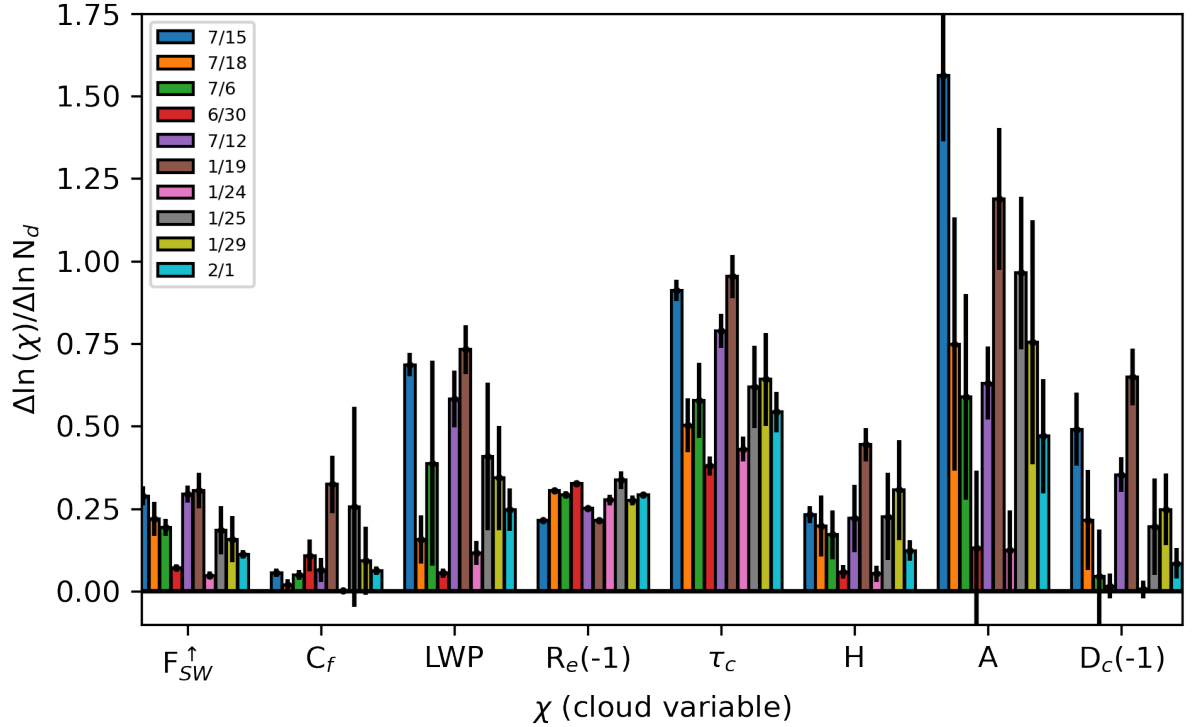


**Figure 10.** Value of the slope in the natural log change of a given variable ( $\chi$ ) with respect to the natural log change in cloud droplet number concentration ( $N_d$ ) computed from 4 aerosol WRF experiments simulations in 10 different case studies (7/15, 7/18, 7/6, 6/30, 7/12, 1/19, 1/24, 1/25) represented at 13:00 UTC.  $\chi$  variables shown are the top of atmosphere outgoing shortwave flux ( $F_{SW}^{\uparrow}$ ), liquid cloud fraction ( $C_f$ ), liquid water path (LWP), effective droplet radius ( $R_e$ ), cloud optical thickness ( $\tau_c$ ), cloud geometrical thickness (H), cloud object area extent (A), and distance between cloud object centroids ( $D_c$ ). Multiplication of -1 on  $R_e$  and  $D_c$  was carried out to make all quantities positive across the bar chart. Uncertainties are represented by the 1-sigma error of the regression fit between quantities.

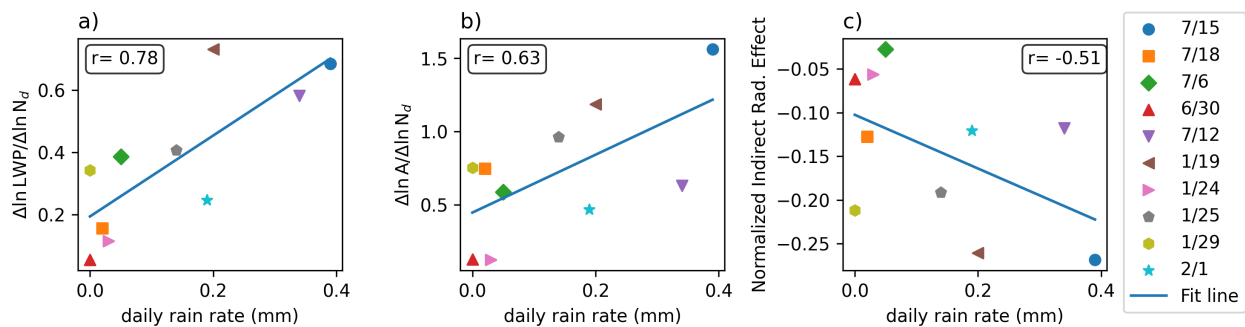


**Figure 11.** Scatter plot of the a) change in liquid water path ( $\frac{\Delta \ln L}{\Delta \ln N_d}$ ), b) change in cellular cloud area as a function of  $N_{d,c}$ , and c) normalized indirect radiative effect which constitutes the Twomey +  $LWP_{adj.}$  +  $CF_{adj.}$  as a function of daily accumulated rain rate from ARM for simulations  $\pm 3$  hours from the time the trajectory intersects Graciosa Island for each case study day, designated by a different symbol as shown in the legend.

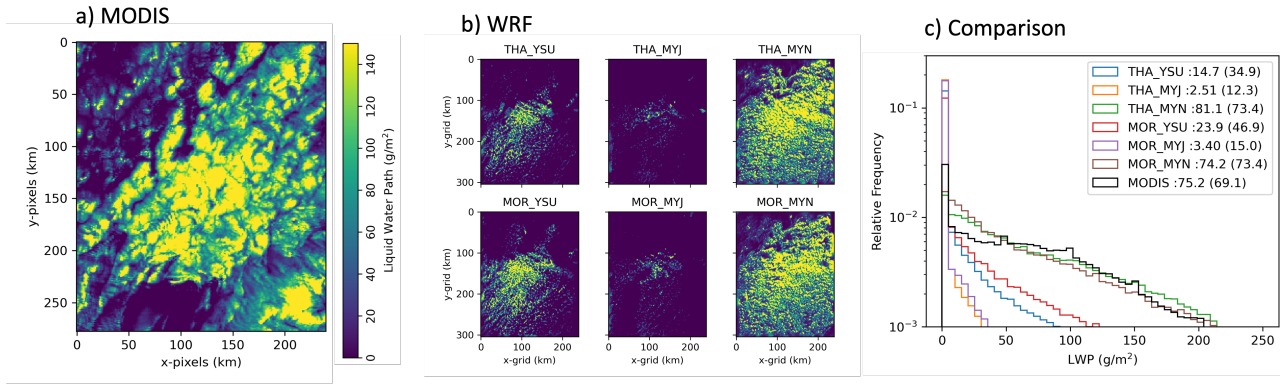


**Figure 12.** WRF control experiments using combinations of the Thompson (THA), Morrison (MOR), Yonsei University (YSU), Mellor–Yamada–Janjic (MYJ), and Mellor–Yamada–Nakanishi–Niino (MYN) boundary layer schemes. Spatial distributions of the liquid water path (LWP) is shown over the for (a) MODIS retrieval of liquid water path at retrieved using the 3.7- $\mu$ m channel at 14:40 UTC, (b) WRF inner domain at 13:00 UTC, and (c) a histogram of the LWP for each experiment and MODIS data. Values in the legend of combination (c) represent with means and standard deviations for each experiment combination displayed.

**Table 1.** WRF model schemes used to study aerosol-cloud interactions. Values for the coinciding names denote the option number used in WRF.

WRF scheme	Value	Name
microphysics	28	Thompson (aerosol-aware)
radiation	4	RRTGM
cumulus	6	Tiedtke
pbl	6	MYNN
sfclay_physics	2	eta similarity
surface physics	2	Noah Land

**Table 2.** Case studies from ACE-ENA IOP periods used to simulate stratocumulus clouds in WRF. Surface temperature ( $T_s$ ), lower ~~troposphere~~-tropospheric static stability (LTS), free ~~troposphere~~-tropospheric entraining relative humidity at 850hPa (FTH), PBL height (determined from the temperature and humidity sounding), cloud base height (determined from the ceilometer), and daily integrated rainfall determined from ARM distrometer observations. Dominant cloud type following Wood and Hartmann (2006) classification based on satellite imagery inspection are listed.

	$T_s$ [ $^{\circ}$ C]	LTS [K]	FTH	PBL height [m]	Cloud base height [m]	Rainfall [mm]	Cloud type	Precipitation
<b>IOP 1</b>								
6/30/17	20.0	20.0	36	890	950	0	disorganized	non-raining
7/06/17	21.5	20.2	26	1410	1107	0.05	homogeneous	light-rain
7/12/17	22.0	17.2	72	1130	325	0.34	homogeneous	moderate rain
7/15/17	16.0	22.0	60	1530	850	3.9	homogeneous	heavy-rain
7/18/17	22.0	18.2	63	950	682	0.02	closed-cells	non-raining with overlying cloud layers
<b>IOP 2</b>								
1/19/18	16.5	16.0	52	950	816	0.2	open-cells	rain
1/24/18	14.0	18.0	32	1710	1411	0.03	open-cells	light-raining with ice
1/25/18	13.0	19.7	21	1510	1302	0.14	closed-cells	drizzle with ice
1/29/18	15.0	18.1	50	1200	1062	0	disorganized	non-raining
2/01/18	15.0	17.8	41	600	565	0.19	disorganized	drizzle

**Table 3.** Twomey radiative effect ~~and ratio of~~, along with the liquid water path ~~adjustment~~ and cloud fraction ~~adjustment~~ adjustments relative to the Twomey effect ~~computed (calculated~~ using equation 1 ~~for each case study~~), are listed. Mean values across all case studies and ~~all case studies~~ excluding 1/25 due to excessive ~~aerosol-induced~~ cloud growth ~~by aerosol~~ are included in the last two rows.

Case	Twomey ( $\text{W m}^{-2}$ )	$\frac{LWP_{adj}}{Twomey}$	$\frac{Cf_{adj}}{Twomey}$
7/15/17	<del>-107.5</del> <u>-29.9</u>	<del>+1.47</del> <u>1.48</u>	<del>0.55</del> <u>0.53</u>
7/18/17	<del>-98.3</del> <u>-27.5</u>	<del>0.38</del> <u>0.41</u>	0.05
7/6/17	<del>-20.7</del> <u>-5.6</u>	<del>0.13</del> <u>0.11</u>	<del>0.69</del> <u>0.66</u>
6/30/17	<del>-54.2</del> <u>-14.8</u>	0.14	0.24
7/12/17	<del>-92.0</del> <u>-24.0</u>	0.48	<del>0.21</del> <u>0.20</u>
1/19/18	<del>-49.5</del> <u>-10.0</u>	<del>+1.61</del> <u>1.58</u>	<del>0.61</del> <u>0.64</u>
1/24/18	<del>-23.0</del> <u>-4.7</u>	<del>0.31</del> <u>0.37</u>	<del>0.015</del> <u>0.01</u>
1/25/18	<del>-17.6</del> <u>-4.1</u>	<del>0.74</del> <u>0.67</u>	<del>4.85</del> <u>3.90</u>
1/29/18	<del>-37.0</del> <u>-7.9</u>	<del>+1.59</del> <u>1.39</u>	<del>+1.65</del> <u>1.29</u>
2/1/18	<del>-39.4</del> <u>-8.5</u>	<del>0.57</del> <u>0.55</u>	<u>0.54</u>
Mean (all)	<del>-53.9 ± 10.6</del> <u>-13.7</u> <u>± 9.3</u>	<del>0.74 ± 0.55</del> <u>0.72 ± 0.53</u>	<del>0.94 ± 1.37</del> <u>0.81 ± 1.09</u>
Mean (excluding 1/25)	<del>-57.9 ± 11.0</del> <u>-14.7</u> <u>± 9.2</u>	<del>0.74 ± 0.6</del> <u>0.72 ± 0.56</u>	<del>0.51 ± 0.47</del> <u>0.46 ± 0.37</u>

**Table 4.** WRF model setup for control and sensitivity experiments. Values in parenthesis denote the option number used in WRF. Experimental setup primarily used for analysis of detailed aerosol-cloud interaction experiments is listed in bold.

Experiment name	Microphysics	PBL
THA_YSU	Thompson (28)	YSU (1)
THA_MYJ	Thompson (28)	MYJ (2)
<b>THA_MYN</b>	Thompson (28)	MYNN3 (6)
MOR_YSU	Morrison (10)	YSU (1)
MOR_MYJ	Morrison (10)	MYJ (2)
MOR_MYN	Morrison (10)	MYNN3 (6)